ABSTRACT

Title of Thesis:	PERFORMANCE OF AMMONIA CONDENSER PLATE TYPE HEAT EXCHANGER
	Andrew Rivera, Master of Science, 2016
Thesis Directed By:	Research Professor Yunho Hwang, Ph.D. Department of Mechanical Engineering

In this study, I experimentally analyzed the performance of a commercial semi-welded plate type heat exchanger (PHE) for use with ammonia systems. I determined performance parameters such as overall heat transfer coefficient, capacity, and pressure drop of the semi-welded PHE. This was analyzed by varying different parameters which demonstrated changes in overall heat transfer coefficient, capacity, and pressure drop. Both water and ammonia flow rates to the semi-welded PHE were varied independently, and analyzed in order to understand how changes in flow rates affected performance. Inlet water temperature was also varied, in order to understand how raising condenser water inlet temperature would affect performance. Finally, pressure drop was monitored to better understand the performance limitations of the semi-welded PHE. Testing of the semi-welded will give insight as to the performance of the semi-welded PHE in a potential ocean thermal energy conversion system, and whether the semi-welded PHE is a viable choice for use as an ammonia condenser.

PERFORMANCE OF PLATE TYPE HEAT EXCHANGER AS AMMONIA CONDENSER

By

Andrew Rivera

Thesis submitted to the Faculty of the Graduate School of the
University of Maryland, College Park, in partial fulfillment
of the requirements for the degree of
Master of Science
2016

Advisory Committee:
Research Professor Yunho Hwang, Chair
Professor Aristos Christou
Associate Professor Bao Yang

Dedication

To my parents, friends, and family who supported me throughout my graduate school career. A special mention to my lab manager Jan Muehlbauer, who taught me everything I needed to succeed, and inspired me to only show my best work.

Acknowledgements

Working for CEEE has played such a crucial role in the progression of both my academic and industrial career, that I would like to acknowledge all of the faculty and staff that worked at this department who guided, inspired, and pushed me to succeed. I could not be more thankful for all the advice, expertise, and professional opinions I was offered along my journey by the members here at CEEE.

I would like to pay gratitude to my advisor, Dr. Yunho Hwang, who granted me the opportunity to reach this level. His vast knowledge and expertise in this field although intimidating, served as motivation to constantly prove myself and make sure I conducted research to the best of my ability to match his standards. I would also like to deeply thank Dr. Radermacher, without whom I would have never been granted the opportunity, and whose insightful advice aided in my research.
A largely deserved thank you goes to my lab manager Jan Muehlbauer, who's incredible knowledge of systems and working practices guided me to become the engineer I am today. One final thank you to all the members of CEEE who made my journey here incredibly unique.

The time I spent at CEEE helped me gain valuable insight into construction, testing, research. It also helped me to understand how to work as part of a team, how to delegate, and how to work on my own when needed. The lessons I learned at CEEE will always keep my work standards high, and push me to exemplify this in all of my future work.

Table of Contents

List of Tables

List of Figures

List of Abbreviations

Symbols

A	Active heat transfer area [m^2]
Ac	Cross sectional flow area [m^2]
b	Corrugation depth [m]
β	Chevron angle [°]
cp	Specific heat [$kJ \cdot kg^{-1} \cdot K^{-1}$]
Δ	Delta (difference between two numbers)
ϵ	Energy Balance [%]
Υ	Channel aspect ratio [ϕ]
h	Enthalpy [$kJ \cdot kg^{-1}$]
λ	Corrugation pitch [m]
Lp	Plate length [m]
LMTD	Logarithmic mean temperature difference [K]
$\dot{m}$	Mass flow rate [$kg \cdot s^{-1}$]
ω	Uncertainty
P	Pressure [kPa]
$\dot{Q}$	Heat transfer capacity [kW]
T	Temperature [°C]
t	Thickness [m]
U	Heat transfer coefficient [$W \cdot m^{-2} \cdot K^{-1}$]
w	Plate width [m]

Acronyms

BPHE	Brazed plate heat exchanger
DAQ	Data Acquisition System
EXV	Electronic expansion valve
HTC	Heat transfer coefficient
HVAC	Heating, ventilation, and air-conditioning
MFR	Mass flow rate
NH_3	Anhydrous Ammonia
OTEC	Ocean thermal energy conversion
PHE	Plate heat exchanger
PID	Proportional-integral-derivative
PTFE	Polytetrafluoroethylene
VCC	Vapor compression cycle
VFD	Variable frequency drive
RTD	Resistance Temperature Detector

Subscripts

avg	Average
c	Cold side
cond	Condenser
evap	Evaporator
i	In
min	Minimum
max	Maximum
o	Out
r	Refrigerant
stdev	Standard deviation
w	Warm side

1. Introduction

1.1 Current Energy Use and Renewables

1.1.1 Worldwide Energy Consumption

Global energy trends display a worryingly constant trend of increase in world energy consumption over the past several decades. Even though appliances and power plants become more efficient, the earth's population continues to grow, undeveloped countries become industrialized, and energy consumption rates continue to rapidly increase. As stated by the International Energy Agency (IEA), a twelve year span from the year 2000 to 2012 saw world energy consumption increase by 47.5%. In 1980, world-wide energy consumption totaled 8,018 billion kWhrs, while later in 2012 it totaled 21,530 billion kWhrs, an increase of 168% in the course of 32 years. Global consumptions trends increase concerns in rapidly emerging economies, such as China who saw a 206% increase in consumption in a short ten year span from 2002 to 2012 (IEA). In order to account for the rapid increase in energy use, the fastest solution was to establish high-pollution energy sourses such as coal burning power plants as the primary energy source. Even with increases in technology, international energy agency (IEA) projects world energy consumption to increase 56% by 2040 alone, due to emerging developing nations, and an increase in population. The increase in energy usage rates and the push towards cleaner, less-polluting options has seen a shift in energy generation towards renewable energy sources. The main contributors are solar, wind, hydro-electric, and bio-fuels. The main focus is to reduce the strain placed on the earth's limited resources, and focus on using resources that are constantly being replenished to provide some of the world's energy

requirements. Future improvements in renewable energy sources will slowly see them gain popularity, as production and technology costs gradually decrease. IEA estimations in 2011 stated that approximately 21% of all global energy generation was accomplished with renewables, and that is projected to increase slowly to 25% by 2040. In the United States alone, hydro power compromises 6% of total energy produced, while all other sources of renewables combined make up 7%. Thus, using hydro power has large incentives, as the ocean is a constant source of clean, renewable energy. This opens the opportunity for energy production sources that utilize the oceans, such as the OTEC system, which utilizes the natural temperature gradient of the water to drive a power cycle. This is incredibly beneficial for small tropical islands, which struggle to generate their own power, and will be able to generate constant, clean energy with the introduction of the OTEC power cycle. Based upon IEA data, the average monthly cost of electricity per kWhr in 2015 was 10.18 cents per kWhr, whereas the island of Hawaii had the highest cost, at 29.94 cents per kWhr, nearly triple the average national price. Introduction of renewable energy cycles that take advantage of naturally available resources such as OTEC can not only produce cheaper electricity for smaller islands, but also consistently produce electricity that reduces production from other non-renewable energy sources.

1.1.2 Ocean Thermal Energy Conversion

Ocean Thermal Energy Conversion (OTEC) refers to the generation of power from a cycle driven by the ocean's natural temperature gradient. Similarly to a conventional power cycle, two heat exchangers, a pump, and an expansion turbine are used. The

hot and cold sources used however are the oceans in tropical climates, where the high water surface temperature (~25°C) is used to evaporate a working fluid, and the low-end cold water sources (~5-10°C) is then used to condense it as stated by William H. Avery (2004). The turbine is then directly connected to a generator which produces electricity for small tropical islands, which otherwise have no readily available power plants for cheap electricity production, as shown in Figure 1. Figure 2 and Figure 3 display P-h diagrams of the proposed OTEC power cycles, both with use with working fluid R-717. The area of interest and focus on both will be on the condenser low-side performance. Figure 2 displays a general P-h diagram, while Figure 3 shows a similar graph, but with appropriate working pressures and temperatures as in the OTEC cycle.

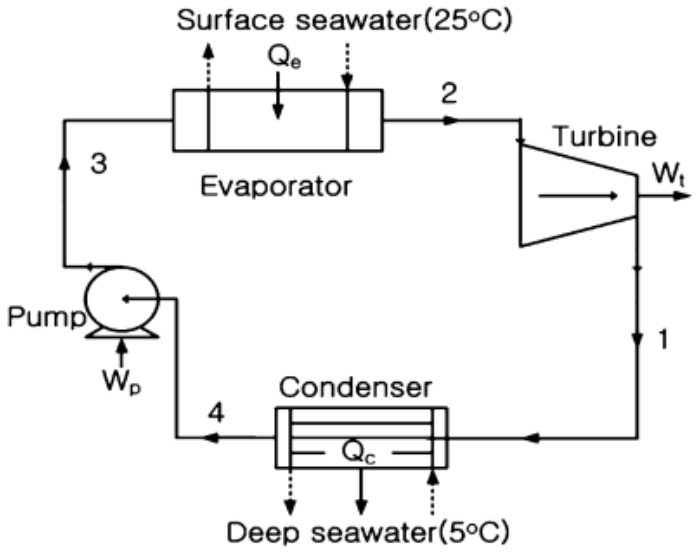

Figure 1: OTEC power cycle schematic (Wu, 2004)

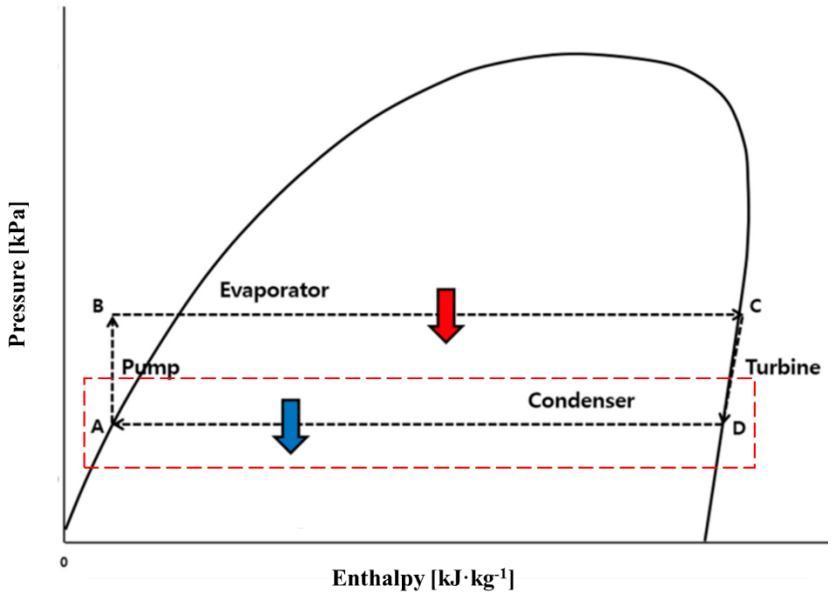

Figure 2: Power Generation P-h Diagram of R-717

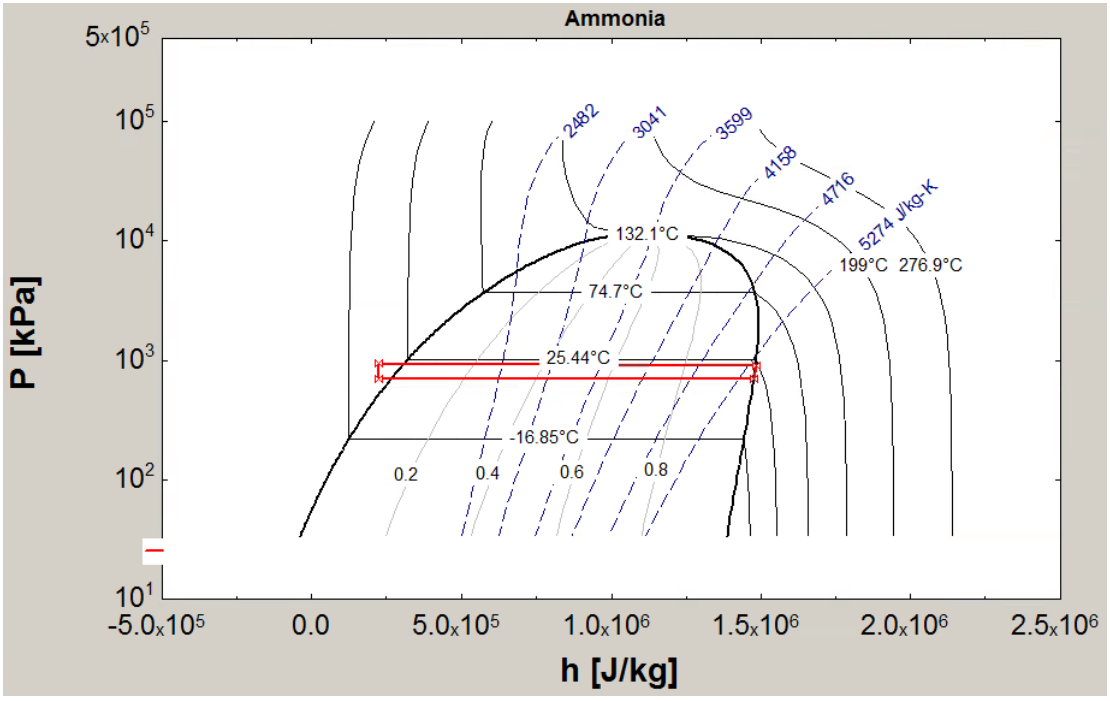

Figure 3: P-h Diagram for OTEC Test Conditions

Utilizing the oceans as a heat source and sink is extremely economical and non-intrusive, as the oceans are a stable energy source that are naturally replenished during the day and night cycles. The ocean bodies are also vastly immense, meaning utilizing water from the surface and ocean floor will have little to no impact on the surrounding wildlife or natural ocean patterns. The typical working fluid utilized in this system is R-717 (ammonia), as it yields very high thermal efficiency when compared to other working fluids, with the added benefit of having zero global warming potential (GWP), and zero ozone depletion potential (ODP) due to it being a natural working fluid. The main drawback to utilizing the OTEC cycle however is the low cycle efficiency (2-3%), due to the small temperature difference seen from the warm to cold water sides. Propositions to increase this efficiency describe implementation of a regenerator, re-heater, and multistage turbine in order to boost the surface water temperature to higher than 25°C. Lee et al. (2011) summarized that a plant utilizing these upgrades could see a large increase in cycle efficiency, seeing it reach realistic values of 5-6%.

Utilization of the OTEC power cycle for islands where electricity generation is difficult or not cheap can provide cheaper, easier access to a mostly renewable, environmentally friendly, and constant energy source due to its high capacity factor of 90-95%.

1.2 Plate Type Heat Exchanger (PHE)

1.2.1 Plate Type Heat Exchanger Overview

When compared to other similar heat exchanger types such as the shell-and-tube, the plate type heat exchanger (PHE) provides more heat transfer area, have greater thermal performance, as well as having a more compact design. A PHE has the advantage of using the complex geometry in the plates to induce more turbulence, as well as having a large heat transfer area per volume and a large thermal effectiveness. The corrugated nature of the plates aids in causing turbulent mixing of the working fluid, and can help to induce secondary flow, thus increasing the amount of heat transferred.

Many different types of plate heat exchangers exist, including brazed plate heat exchangers (BPHE), semi-welded PHE's, shell-and-tube, and traditional gasketed plate-frame PHE's. The plate-frame gasketed type utilized plates arranged in cartridges that are sealed by use of an elastomer gasket. This allows for easy and fast disassembly and re-assembly, however the gasket materials are subject to corrosive working fluids and high pressures, where leaks can develop rapidly. Brazed plates (BPHE) shown in Figure 4 use brazing to keep the plates together, which allow them to withstand the higher pressures and corrosive working fluids better than the conventional plate-frame gasketed type.

Figure 4: Brazed PHE

The shell-and-tube type shown in Figure 5 utilize a plate pack which is welded and assembled inside of the outer shell, which helps to offer high heat transfer capabilities in very small spaces.

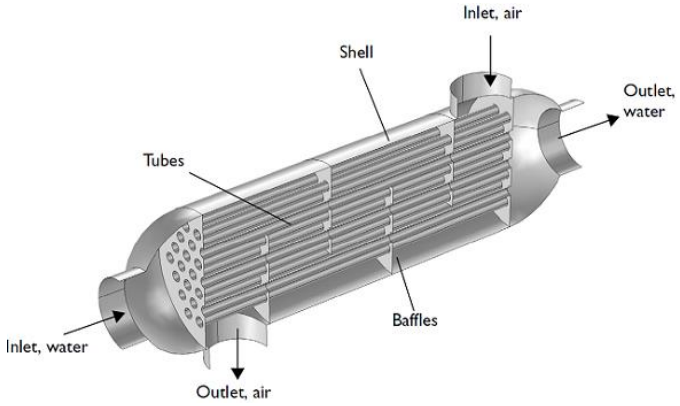

Figure 5: Shell-and-Tube PHE

Semi-welded PHE uses two one-sided plates laser welded together to form one cassette as shown in Figure 6.

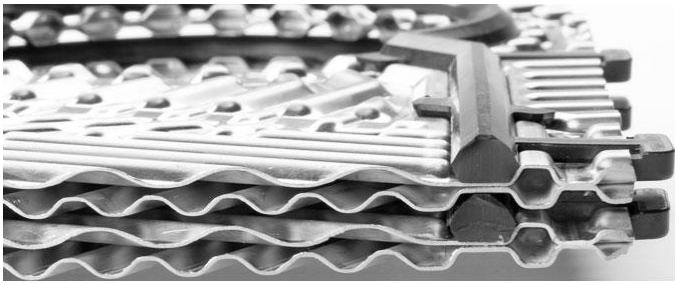

Figure 6: Semi-welded PHE plates (Alfa-Laval)

The cassettes are then arranged in series, one over another with a front and end plate to complete the PHE. The laser welding vastly increases the strength of the seals, which can handle higher pressure without fear of leaks. It offers high heat transfer performance, versatility, and low volume usage, thus making it one of the best currently existing options. Each heat exchanger variant serves different purposes and has advantages and disadvantages, and for practical and efficiency purposes, the semi-welded type was chosen for the following tests.

1.2.2 Semi-Welded PHE

Differing from a conventional gasketed PHE, the semi-welded PHE utilized two plates (front and back) which are laser welded together to form a single cassette. The two sides form an interior refrigerant flow channel, shown in red arrows in Figure 7.

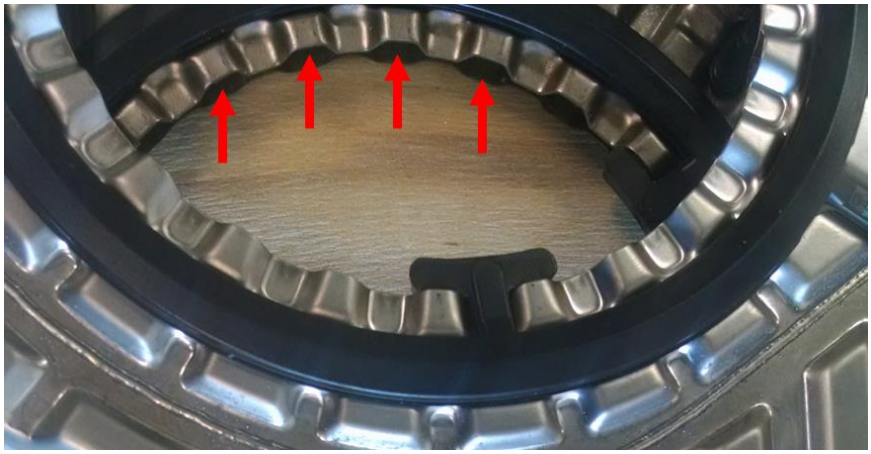

Figure 7: Refrigerant Flow Channels in PHE

Each cassette is then stacked sequentially, until the desired capacity is reached for the PHE. Working fluid flow through each cassette to the next is connected by refrigerant-side gaskets, typically made from a chemical and corrosion resistant Teflon or elastomer polymer. Each cassette (front and back) also has a water-side gasket, as shown in Figure 8.

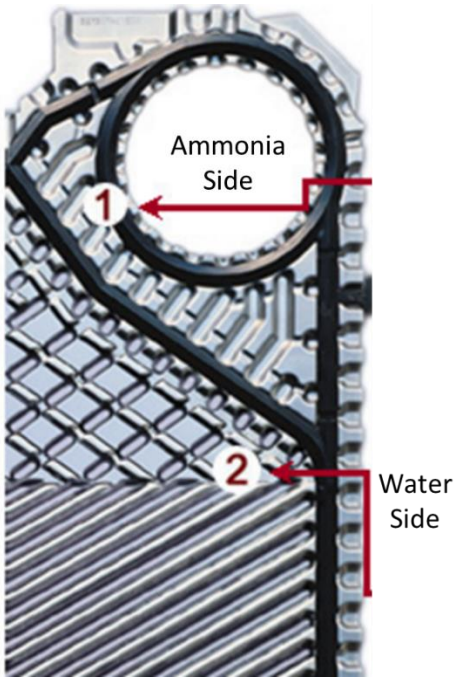

Figure 8: Plate with gasket separation

This ensures that water travels only along the designated path outlined by the gasket, and does not interfere with the ammonia side gaskets.

The type used in the experiment was an Alfa Laval M10BW-FD, as shown in Figure 9.

Figure 9: Alfa-Laval M10BW-FD PHE

The PHE had a total of 40 cassettes, including the front and end plates. The flow patterns is shown in Figure 10, where the unit was operated in counter-flow, with working fluid entering from the top and exiting from the bottom (as it was a condenser).

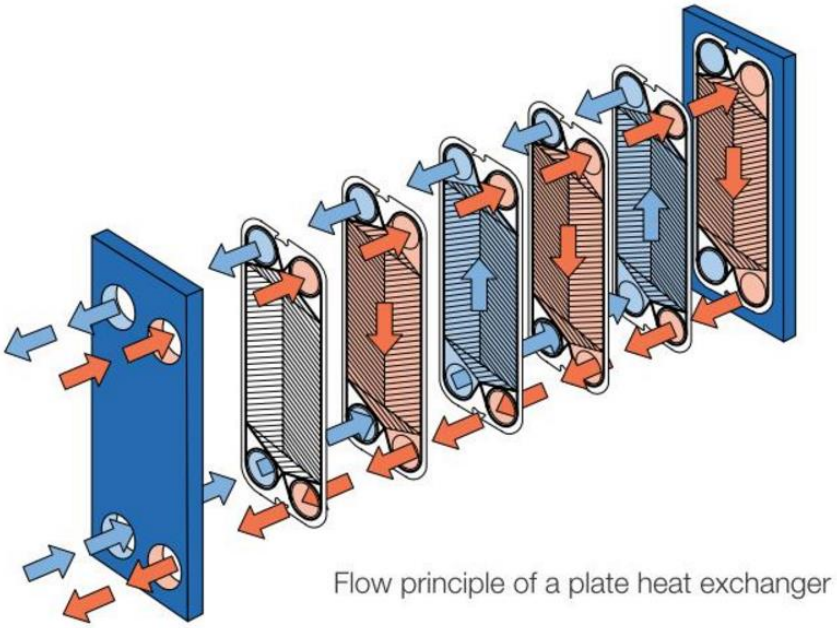

Figure 10: Working fluid Flow Direction PHE

Cold water was pumped into the bottom, and exited from the top, allowing for perfect counter-flow to occur, which is proven to have better heat transfer when compared to parallel flow. Table 1 summarizes the configuration parameters used in testing of the PHE condenser.

Table 1: PHE specifications

Parameter	**Value**
Height [cm]	108.5
Width [cm]	47.0
Depth [cm]	24.64
Design Pressure [MPa]	2.5
Design Temp [°C]	-50 – 180
Material type	Titanium
Plate count [EA]	40

1.2.3 Geometry of Semi-welded PHE

The increased performance of the PHE when compared to other heat exchanger types is primarily due to the complete geometry present on the plate surfaces. A commonly used plate geometry is denoted as chevron type, dictated by the sinusoidal shape of the corrugations which run along the plates, shown in Figure 11

Figure 11: Plate Sinusoidal Shape Geometry

Many geometrical factors influence the heat transfer performance of the PHE, mainly parameters such as plate length (L_p), plate width (W), the chevron angle (β), the spacing between individual corrugations (λ), and the corrugation depth (b), all of which are shown in Figure 12.

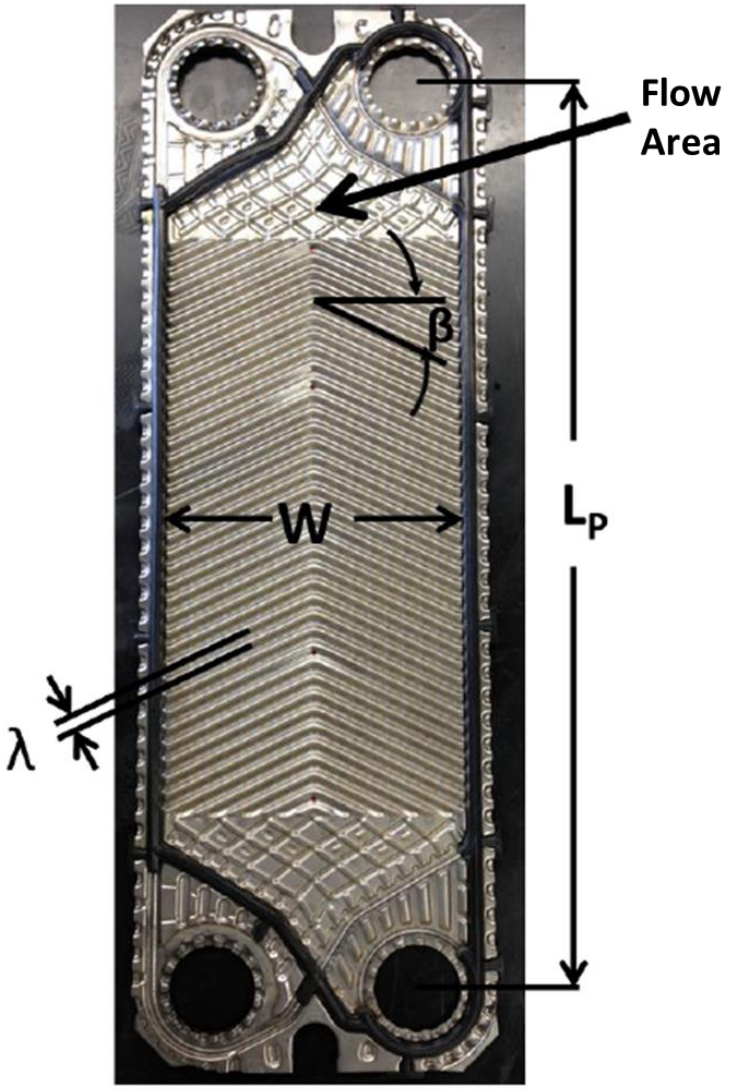

Figure 12: Plate Parameters and Geometry (Li, 2012)

Two types of chevron angles exist, denoted soft and hard angles, which determine how the chevron angle affects heat transfer performance and pressure drop, based upon findings by Martin (1996) and Khan et al. (2012). Typically, the chevron angle β is defined as the angle formed between the corrugation passes and the direction orthogonal to the flow. In their conducted studies, low chevron angles (otherwise denoted as hard angles) provide high thermal performance and efficiency, at the cost

of increased pressure drop, whereas high or soft angles provide lower pressure drop, but also decreased thermal performance of the plates. The corrugation on the plate surfaces aids in inducing turbulent flow for all Reynolds numbers (even low ones), and also aids in increasing heat transfer area and helping with even fluid flow distribution. As explained by Han et al. (2010), the irregularity of the corrugations causes the flow region to continuously contract and expand, which causes a constant change in flow direction, more readily inducing turbulent flow. Faizal (2012) also emphasized that once the hydraulic layer has fully developed for smooth surfaces, the central region of the plate wall does not transfer heat. Thus, plate corrugation aids in inducing secondary flow to enhance the heat transfer that would not be present without corrugation.

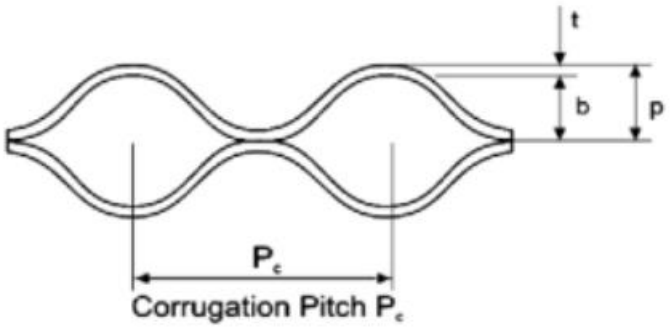

Figure 13: Corrugation Depth

The corrugation depth (b) as shown in Figure 13 displays the flow area available for pathing of fluid, which also takes into account the plate thickness (t). Plate depth (b) is defined as:

$$b = p - t \quad \textbf{(1)}$$

"P" represents the total depth of the half-plate, from the top of the corrugation until the middle. Depth (b) is then calculated by subtracting the plate thickness (t). Cross sectional area (A_x) can then be calculated once a value has been obtained for corrugation depth and plate width (w) is known.

$$A_x = b * w \quad \textbf{(2)}$$

In order to accurately determine hydraulic diameter (d_h), the enlargement factor (ϕ) must first be determined. This is calculated using the perimeter (P), but in cases where corrugation depth is smaller than plate width (Ayub, 2003), the equation simplifies as follows:

$$P = 2(b + w\phi) \approx 2w\phi \quad \textbf{(3)}$$

From this equation, hydraulic diameter (d_h) is defined by:

$$d_h = \frac{2b}{\phi} \quad \textbf{(4)}$$

The enlargement factor (ϕ) is defined as the ratio of developed dimension to protracted dimension, as shown by Figure 14.

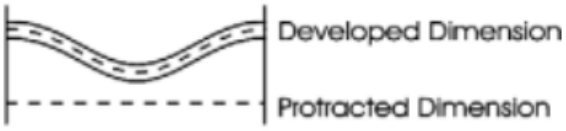

Figure 14: Enlargement Factor Representation

Once the value for enlargement factor (ϕ) is obtained, it can be used to calculate the hydraulic diameter (d_h).

1.3 Heat Transfer Performance of PHE

Heat transfer performance of plate type heat exchangers based upon chevron angle, heat flux, mass flux, and quality has been analyzed and tested by many researchers, with conclusive findings. Justus et al. (2009) discovered a very strong correlation between refrigerant mass flux, chevron angle, and heat transfer coefficient (HTC). As mass flux was increased, HTC was also increased, albeit at different rates based upon lower chevron angles (highest HTC), and high chevron angles (lowest HTC). He also analyzed the effect of vapor quality on HTC, and concluded that when vapor quality was decreased, HTC decreased rapidly as well. At high qualities near one, chevron angle contributed substantially to the HTC, but when vapor quality was decreased, this parameter hardly effected HTC at all. Similarly for pressure drop, as vapor quality was decreased, pressure drop followed the same trend and decreased linearly.

A different study conducted by Huang (2012) displayed the effects of heat and mass flux, vapor quality and chevron angle as well, and its effects on BPHE performance. Huang (2012) discovered a dissimilar result, where the HTC had a strong correlation to heat flux, but a weak correlation to mass flux, quality, and chevron angle. His explanation of tests conducted with R-134a concluded that heat flux was controlled by nucleate boiling in the dominant mode.

In comparison to the previous two studies, Han et al. (2003) also tested heat transfer performance of R-22 and R-410A refrigerants in a BPHE, where parameters such as

heat flux, mass flux, vapor quality, and chevron angle were varied to monitor effects on performance. They discovered that was vapor quality increased, HTC also increased as also shown by Justus et al. (2004). For regions with low quality, it was observed that heat transfer became more sensitive to heat flux, and this was attributed to nucleate boiling being more dominant in this region than convective boiling.

Contrary to the tests conducted by Justus et al. (2004), Li (2012) conducted tests varying vapor quality of a semi-welded PHE to discover that vapor quality has little to no significant impact on heat transfer coefficient (HTC), although a small decrease was shown when vapor quality reaches a value of one. He discovered that HTC increased in cases where saturation pressure was low, and also stated that mass flux was not a factor affecting HTC at vapor qualities lower than 0.5, but showed an increase in HTC at vapor qualities greater than 0.5.

Although many researchers have already analyzed the heat transfer performance of BPHE's with standard working fluids, not much work has been conducted in analyzing performance of a semi-welded PHE used as a condenser with a natural working fluid (ammonia).

1.4 Working Fluid Selection

Working fluid selection plays a pivotal role in both the OTEC power generation cycle, as well as the experimental cycle that will replicate the water inlet and outlet conditions. Thus, a working fluid which exhibited evaporation characteristics around 25°C and condensing around 10°C with medium to low pressure was required. R-717

(ammonia) was selected for the experimental test, as it emulates the working fluids used in the OTEC cycle, providing very high levels of heat transfer per gram of flow rate, as well as having zero GWP and zero ODP, shown in Table 2.

Table 2: Working Fluid ODP and GWP (Linde Gases AG)

Fluids	Physical data	Environmental data	
	M (g/mol)	ODP	GWP (100 years)
R22	86.48	0.05	1,600
R134a	102.03	0	1,430
R717	17.03	0	0
R290	44.1	0	3
R600a	58.12	0	20
R1270	42.09	0	3
R744	44.01	0	1
R245fa	134.05	0	1,030
R227ea	170.03	0	3,320
R236fa	152.04	0	9,810
R410A	72.6	0	1,730
R404A	97.6	0	3,260

[a] ASHRAE 34 safety group

The use of such a working fluid in the OTEC cycle poses no environmental safety hazard to the oceans, as it is a natural refrigerant. The compatibility of the working fluid with the turbine and system was also taken into account, as shown by Figure 15.

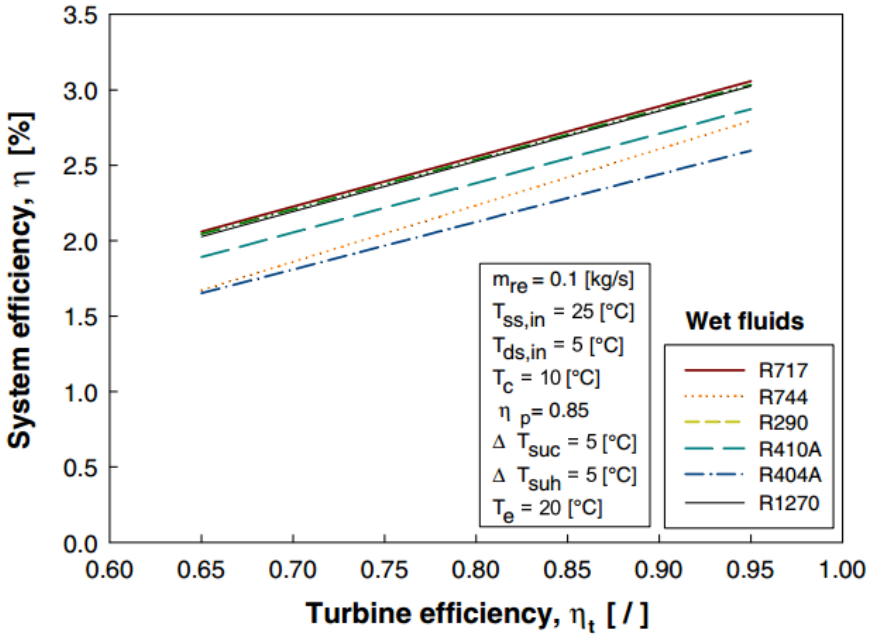

Figure 15: Working fluid Efficiencies in OTEC Cycle (Yoon, 2014)

The largest slope increase in system efficiency is shown by R-744, while the highest system efficiency is shown by CO_2, but due to its extremely high system pressure, it was not selected. The largest contributor to system efficiency was R-717 (ammonia), and due to its low-medium operating pressures and high heat transfer per gram of flow rate, it was well suited for operating in the semi-welded PHE, and thus selected as the working fluid.

1.5 Objectives of Study

Literature review displays many reasons for testing the capabilities of an ammonia PHE for use in an OTEC power generation cycle. As stated by Yoon et al. (2014), even though the OTEC cycle has a very low realistic efficiency (around 3-5%), the hot and cold sources are essential free, as they are provided by the earth's natural ocean temperature gradient. With such a low efficiency system where only pumping

power is required, the two heat exchangers utilized play a pivotal role in keeping as much generation efficiency as possible in the plant. Testing of the plate-type heat exchanger with ammonia will help understand how the OTEC cycle performs with the Alfa-Laval PHE condenser used, where the benefits of using such a PHE lie, and potential drawbacks and issues with performance. Analysis of the PHE condenser by varying three main parameters that will affect overall plant and heat exchanger performance are water-side flow rate, ammonia-side flow rate, and water inlet temperature. Both flow rates in the experimental set-up and real application can have variable flow rates, and those flow rate effects are tested in the experiment. The different flow rates will display how the ammonia condenser operates, in terms of capacity and heat transfer coefficient (U-value). This will give an indication of what flow rate combinations are required for desired performance figures in the OTEC set-up. The final variable of water inlet temperature relates to the variability of the earth's oceans. As every ocean or OTEC location will have a different geographical climate, the water inlet temperature used for the condenser can have some variations, which will be taken into account in the experiment by slightly varying the inlet temperature within a few degrees, as described by Wu (2004). Not taken into account is the variability of the heat exchanger geometry, such as swapping out plates for different chevron angle plates, or increasing/decreasing the number of cassettes. The study primarily focuses on the effects of the three combined variables listed previously, and how do they affect the PHE performance of the condenser. A better understanding of how the PHE performs under various parameter changes will give

insight into maximizing OTEC plant efficiency, reducing energy consumption, and increasing heat transfer across both plate heat exchangers.

2. Experimental Set-up and Operating Procedure

2.1 Test System Schematic

2.1.1 Water Loop

Two main loops drive the cycle, one used for evaporator (heating) and one for condensing (cooling). Both of the PHE's make use of working fluid-water heat transfer, and as such two independent 379 liter water storage tanks were used. Both loops have an individual pump that draws water out of each warm and cold water tank, respectively and pumps it to the appropriate condenser or evaporator heat exchanger. Both pumps feature a highly accurate Coriolis mass flow meter shown in Figure 16 before the inlet to the pump, which effectively measures density, and thus can calculate water mass flow rate, essential for regulating flow rate into each respective PHE in the system.

Figure 16: Coriolis Flow Meter

An electric pool heater shown in Figure 17 with maximum capacity of 54 kW with a corresponding pump was used to provide a regulated temperature of water to the warm water storage tank, which would be the source for the evaporator warm water.

Figure 17: Warm Water Tank with Electric Heater

A second pump, denoted warm water pump removes water from the hot storage tank and pushes it into the PHE evaporator enclosure and across the semi-welded plates, in counter-flow to the working fluid direction. Since evaporator water inlet temperature needed to be held nearly constant, a pair of electric actuators presented in Figure 18 helped the mixing of water exiting the warm water tank and entering the evaporator enclosure. The warm water pump has two different inlet sources, each with its corresponding actuator.

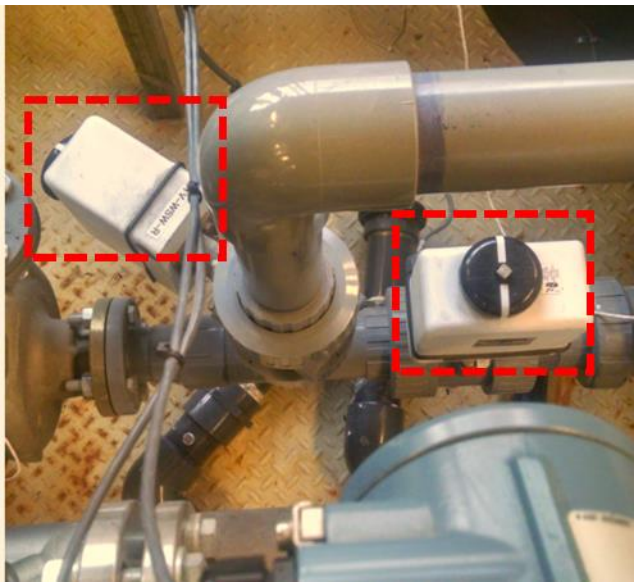

Figure 18: Electric Mixing Actuators

One inlet pulls water directly from the hot water tank, while the other allows water from the evaporator return to re-circulate or mix with the second water inlet stream as desired. The regulation of the actuator openings allows for accurate mixing of the return and hot tank water in order to achieve the desired temperature, which is then fed directly into the warm water pump and sent into the evaporator.

Similarly, the cold water pump removes water from a 379 liter chilled water tank, and pumps it into the PHE condenser at a desired set temperature, as shown in Figure 19.

Figure 19: Cold Water Tank and Coriolis Flow Meter

An outdoor chiller unit shown in Figure 20 with maximum cooling capacity of 105 kW (57.5 kW at tested conditions) was used to pump cooled glycol into a separate water-to-glycol PHE shown in Figure 21, which then sent the cooled water into the cold water storage tank.

Figure 20: Outdoor Glycol Chiller

Figure 21: Water-Glycol Heat Exchanger

Figure 22: Chiller Control

Similar to the hot water tank, a series of electric actuators aid in providing a stable temperature exiting the water tank, as they allow for recirculation of colder water and mixing until the desired temperature for the PHE condenser is reached. Figure 22 shows the chiller control interface, where glycol temperature can be set and controlled.

2.1.2 Working fluid Loop

A retrofitted test facility was slightly altered in order to properly test and analyze the performance of the PHE at various conditions. The system schematic is shown in Figure 23.

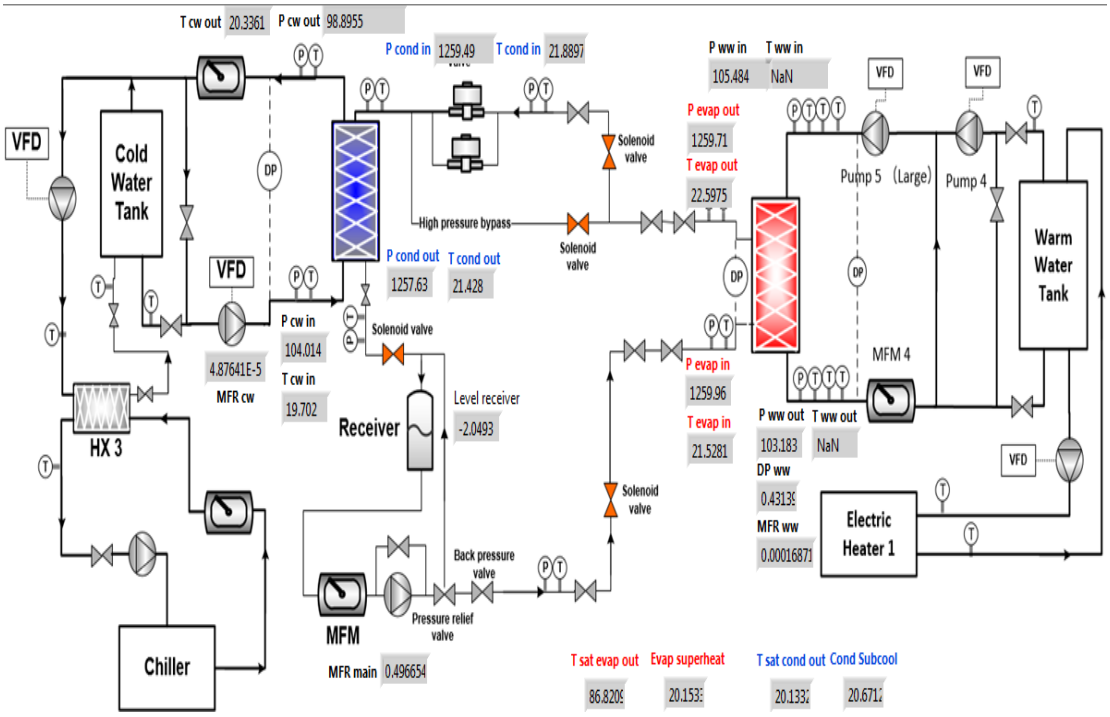

Figure 23: Test System Schematic (LabView)

Figure 23 displays the entire system schematic as displayed in the LabView interface. This shows both warm and cold water loops, as well as the working fluid loop. Shown in the interface are system temperatures, pressures, and flow rates.

Figure 24 shows a close-up of the warm-water side, which includes the evaporator, warm water tank, and pool heater along with various water pumps.

Figure 25 shows a close-up of the cold-water side, which includes the condenser, and similarly shows various inlet and outlet pressures, temperatures, and flow rates.

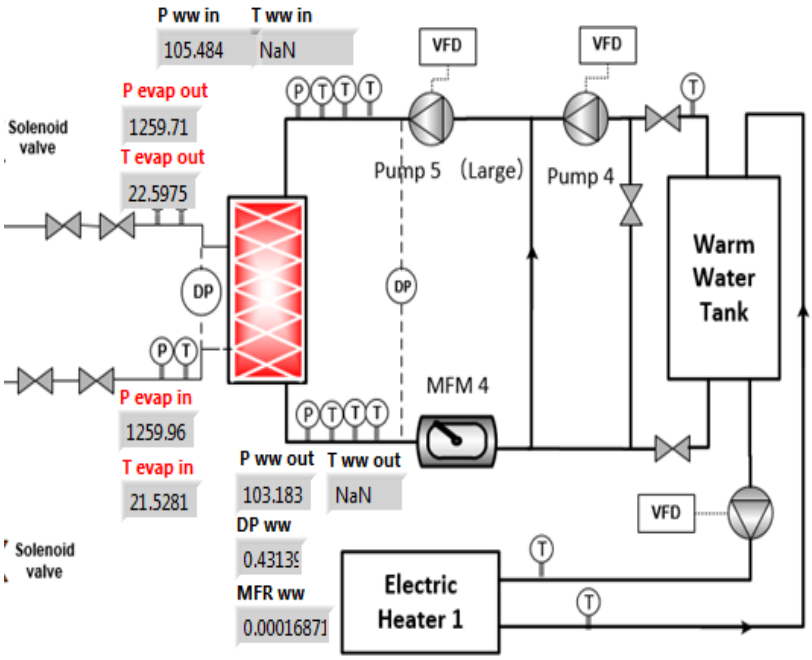

Figure 24: Warm Water Loop

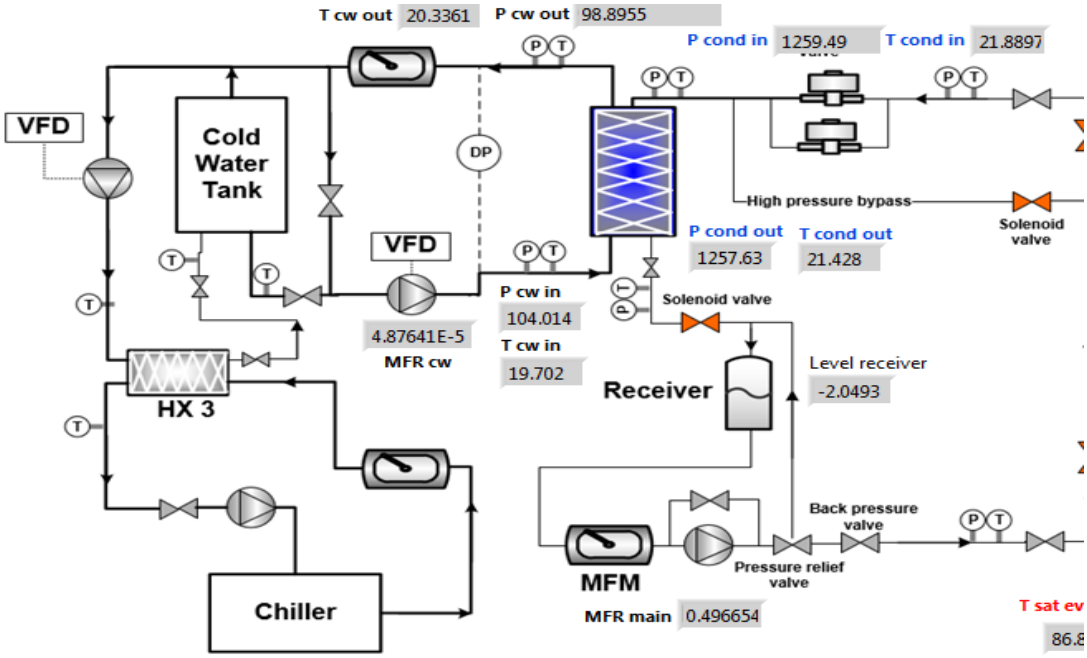

Figure 25: Cold Water Loop

Several ball valves were also installed into the system, in order to minimize refrigerant release in the case of a leak or accident when the system is running. The system set-up differs from that of a typical vapor compression cycle (VCC), as the current test facility was constructed to accommodate testing for a power generation cycle. Whereas in a VCC the evaporators and condensers are on the low and high sides, respectively, the power generation facility uses the evaporator as the high-side unit and condenser on the low-side. Although a normal power generation cycle would include a turbine, the purpose of this test was only to evaluate the performance of the PHE condenser, and as such the turbine was replaced with a standard expansion valve. The electronically controlled expansion valve (EEV) served to expand working fluid vapor and act as the turbine, although all vapor generated through the evaporator was not made use of for any power generation. While a compressor is used in a standard VCC, this system's driving force was provided by diaphragm pump, as standard with many power cycle applications. The pump is controlled by a variable frequency drive as shown in Figure 26 (maximum output of 0.75 kW) allowing for changes in refrigerant mass flow rate as needed for varying test conditions.

Figure 26: Ammonia Pump with VFD Motor

Liquid refrigerant enters the pump, from which it is then pushed through a section of 1.9 cm stainless steel piping, where it enters the PHE evaporator in liquid state. Directly after the pump discharge is a Coriolis mass flow meter, which accurately measures the mass flow rate of the refrigerant due to the high density of the liquid ammonia. Similar to the condenser, the evaporator used was also a semi-welded PHE, but with a different pattern than the condenser. Armaflex 1.27 cm foam was wrapped around the pump discharge lines leading up to the evaporator inlet to minimize heat losses. After exiting the evaporator, the refrigerant enters a pair of valves, one of which was electronically controlled with the assistance of an electronic expansion valve (EEV), displayed in Figure 27.

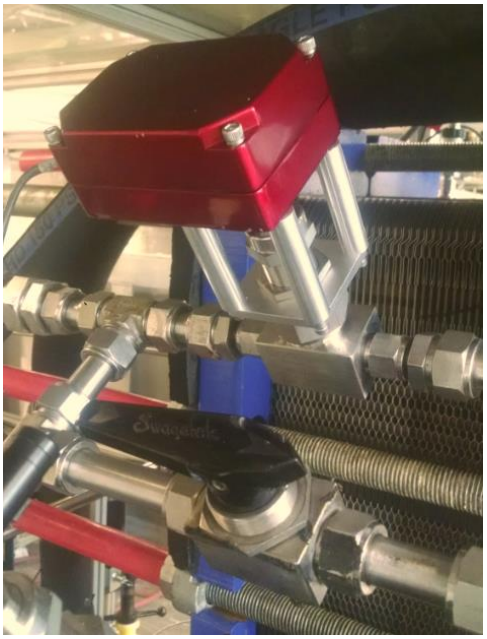

Figure 27: EEV Actuator

This electronic actuator aids in regulating the evaporator high side pressure to desired conditions. The evaporator outlet lines were constructed with 2.54 cm outer diameter stainless steel piping which was then reduced to 1.9 cm when nearing the EEV, in order to reduce pressure drop as vapor or two-phase refrigerant left the evaporator. After expansion through the EEV, the working fluid then entered the semi-welded Alfa Laval PHE condenser as shown in Figure 28 where the entering two-phase or vapor was then condensed into a fully sub-cooled liquid.

Figure 28: Alfa-Laval M10BW-FD PHE Condenser

The condenser outlet lines were completed in 1.9 cm stainless and drained directly into a receiver tank, pictured in Figure 29, which operated between 70%-100% fill capacity in order to ensure adequate liquid feed to the pump.

Figure 29: Ammonia Liquid Receiver

The receiver then feeds directly into the pump with 2.54 cm stainless steel lines, to ensure maximum opening and flow into the pump, which could be limited by smaller piping. The condenser, receiver, and pump were staged at three different decreasing heights, to ensure that liquid drain is aided by the effect of gravity since the pump is only gravity fed, and thus has to be the lowest point in the system. The entire cycle is complete once liquid ammonia reaches the inlet of the pump.

2.2 Data Acquisition System (DAQ) and Instrumentation

2.2.1 Measurement Points and Instruments

The system involved several different measuring devices in order to collect data for pressures, temperatures, and flow rate. The pressure and temperature sensors were placed at the inlet and outlet of each PHE (working fluid side), respectively. These are used for state point and enthalpy calculations, whereas the flow rate coupled with temperature and pressure measurement points was used to calculate PHE capacities.

The pressure and temperature sensors were installed as a pair, either in a side-side configuration, or a top-bottom, as shown in Figure 30.

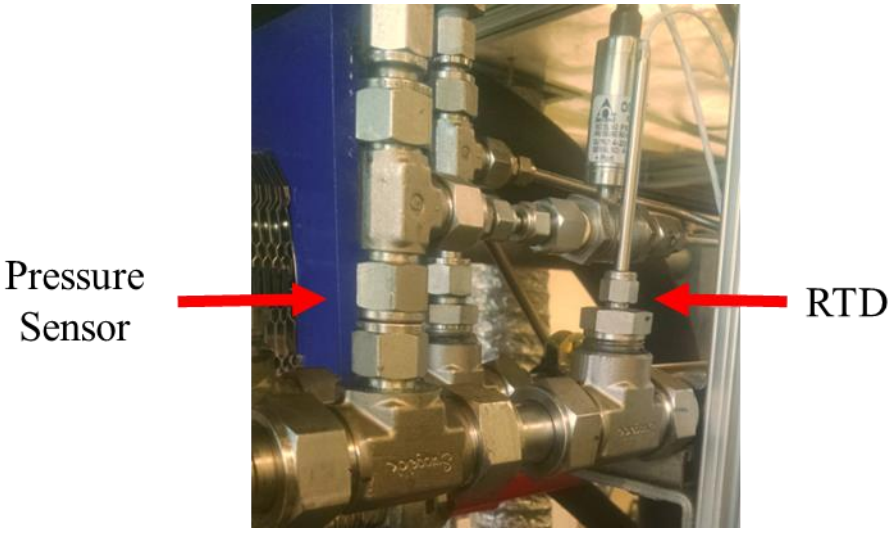

Figure 30: Pressure and Temperature Measurement Coupling

Water-side inlet and outlet temperatures were also measured for each PHE, along with flow rate from a Coriolis flow meter. A table displaying all measurement instruments is shown in Table 3.

Table 3: Test Measurement Instruments

Instrument	Measurement Point	Manufacturer	Model	Type	Sensor Range	Systematic Uncertainty
Mass/Volume Flow Rate	Evaporator Warm Water	Micro Motion	CMF100H	Coriolis	0-3.5 [$kg \cdot s^{-1}$]	0.05%
	Condenser Cold Water	Micro Motion	CMF100H	Coriolis	0-3.5 [$kg \cdot s^{-1}$]	0.05%
	Refrigerant	Micro Motion	CMF025H	Coriolis	0-100 [$g \cdot s^{-1}$]	0.05%
Temperature Sensors (RTD)	All inlet/outlets	Omega	P-M-1/10-1	Resistance Temperature Detector (RTD)	-100-400°C	0.03°C
Pressure Sensors	Evaporator Refrigerant Inlet/Outlet	Wika	S-10	Strain Pressure Transducer	0-1724 [kPa]	0.125%
	Condenser Refrigerant Inlet	Wika	S-10	Strain Pressure Transducer	0-1724 [kPa]	0.125%
	Condenser Refrigerant Outlet	Setra	ASM1200PA2M11B3B00	Strain Pressure Transducer	0-1379 [kPa]	0.05%

2.2.2 System Instrumentation

National Instrument Data Acquisition (DAQ) modules were used to connect all listed instruments and sensors, of which several modules are displayed in Figure 31.

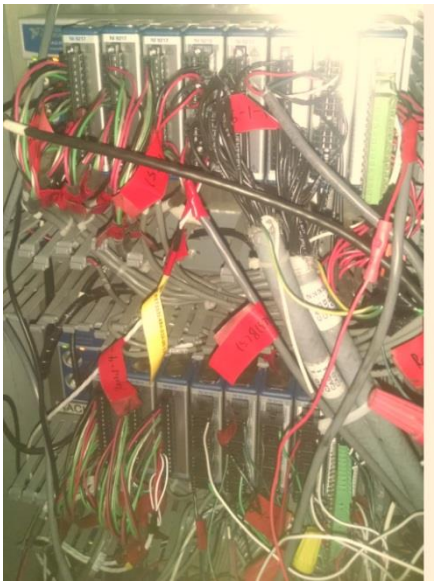

Figure 31: Data Acquisition (DAQ) Modules

The modules used were: NI 9203, 9205, 9217, and 9219 which take either current or voltage readings from all sensors, and then are converted into measureable values. Using a LabVIEW interface, sensor readings with input calibrations were displayed on a system interface, as shown in Figure 32. Control over certain actuators (mainly warm water and cold water mixing) was established by a custom written program in LabView, which made use of a proportional-integral-derivative (PID) algorithm. Figure 32 shows the interface in which a desired value was set for either temperature or mass flow rate, which was then adjusted automatically by LabView until the measurement point matched the desired value set by the user.

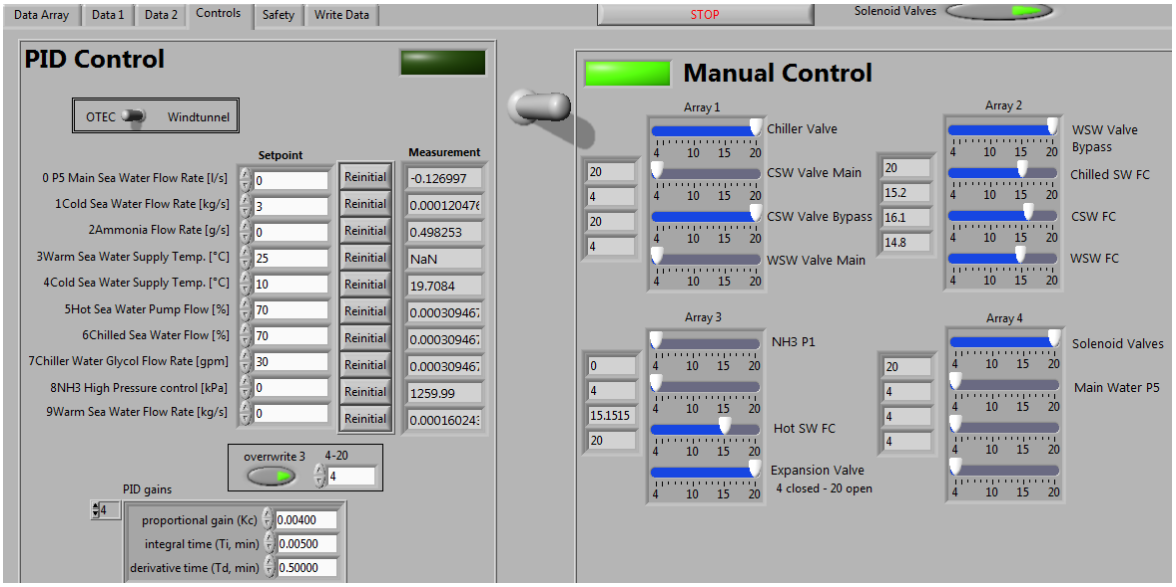

Figure 32: PID LabView Control Interface

The three PID controls in the system regulated warm water inlet temperature (into the evaporator), cold water inlet temperature (into condenser), working fluid mass flow rate, and main water flow rate. Set values were allowed to completely stabilize before data was recorded, to allow for accurate steady state data collection. Data collection for each test was taken for periods of 30 minutes per test.

2.2.3 RTD and Temperature Calibration

Before testing commenced, all newly installed temperature measurement sensors were calibrated in order to have highest accuracy readings. After being connected to their respective DAQ module, RTD's were placed in a highly stable and accurate temperature bath, pictured in Figure 33, which was varied across three different set temperatures. Only three temperatures were used with a total range of 10°C. The range used was extremely small, as evaporator inlet temperature was to be held at a constant 25°C in all tests. Once the bath stabilized at the desired temperature and

RTD's were placed into the bath, one further pre-calibrated high accurate RTD was placed into the bath as well.

Figure 33: Calibration Bath

The measured RTD values were then recorded, and plotted against the high accuracy RTD, where a slope and intercept could be found, which was then used to adjust each sensor to match each other prior to testing. Table 4 shows the data collected used in the calibration for the evaporator water inlet temperatures.

Table 4: RTD Calibration Temperatures

Bath Temperature [°C]	20.0	25.0	30.0
High Accuracy RTD [°C]	20.95	24.98	29.97
RTD-1 [°C]	20.59	25.73	30.87
RTD-2 [°C]	20.55	25.69	30.82
RTD-3 [°C]	20.57	25.7	30.85

Figure 34 displays the slope and y-intercept obtained from plotting one RTD readings versus the high accuracy RTD. This process was repeated simultaneously for all RTD's, and updated equations were entered in LabView program until all RTD's measured within 0.03 °C of each other.

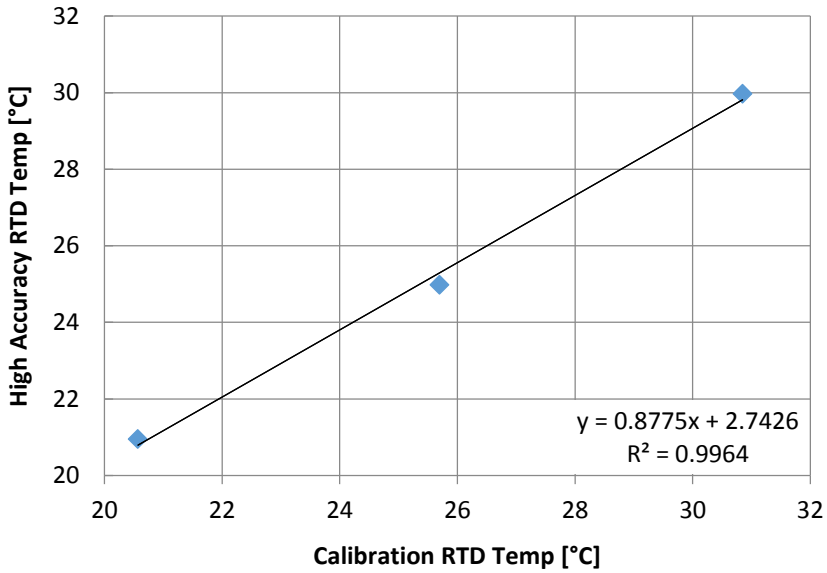

Figure 34: RTD Calibration Slope and Intercept

2.2.4 Differential and Pressure Transducer Calibration

Similar to the temperature calibration, all absolute and differential pressure sensors in the system were calibrated prior to testing. As shown Figure 35, various pressures were put on the system, which was also connected to a pre-calibrated pressure sensor kit, and recorded values of each transducer current in mA was plotted against the high accurate pressure reading. From the intercept and slope, all transducer values were adjusted accordingly until they read within 1% of each other.

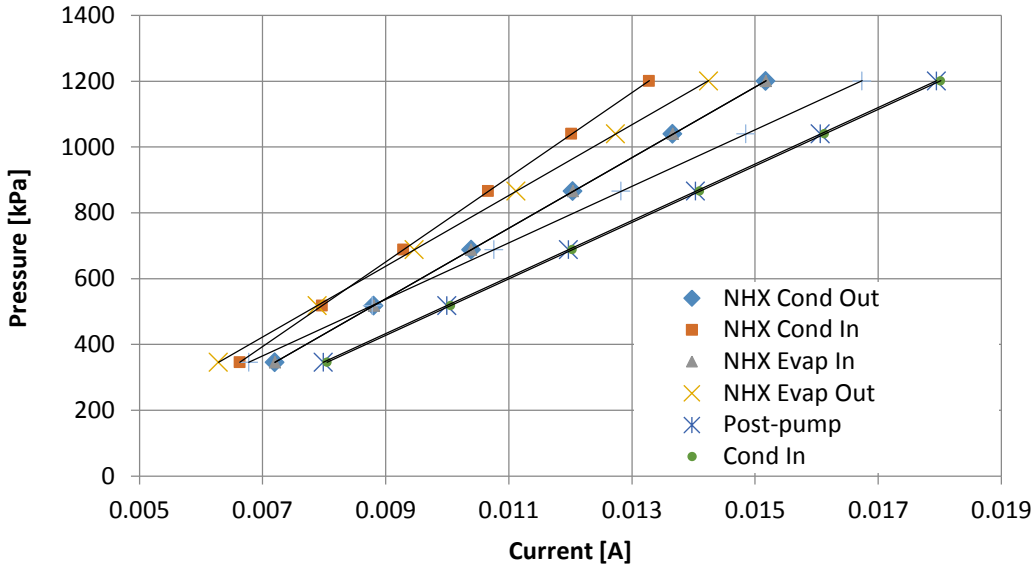

Figure 35: Pressure Sensor Calibration

2.3 Test Conditions and Operating Procedure

As the goal of testing was to analyze the performance (U-value) of the PHE condenser under various operating conditions, a test matrix was established, displayed in Table 5.

Table 5: Test Matrix

$\dot{m}_{water}$ [kg·s^{-1}]	$\dot{m}_{ammonia}$ [g·s^{-1}]	$T_{water_{inlet}}$ [°C]
2.5	30, 32, 34, 36, 38, 40,42	8
3.0	30, 35, 40	8, 10, 12
2.0, 2.25, 2.5, 2.75	40	8

Water-side flow rate was varied from 2.0 kg·s^{-1} up to nearly the maximum pump output of 3.0 kg·s^{-1}. Ammonia flow rate was also varied in each test from 30 to 40 in increments of 5 g·s^{-1}. Cold water inlet temperature was also increased to establish a correlation of PHE performance based on the changing three variables. The final set

of tests where ammonia flow rate was increased by only 2 $g \cdot s^{-1}$ per test were completed to accurately determine the point where superheating fails to exist at the evaporator outlet, and two phase exits the rather than superheated vapor. This is critical to the energy balance calculations for evaporator and condenser, for both water-and working fluid-side.

Prior to testing, extensive leak checking on refrigerant side was conducted, which included all sections where working fluid would pass through. Once the system was determined leak-tight (pressure tested to 1,250 kPa), refrigerant charge was added until system receiver showed at minimum of 80% liquid fill. This ensured that condenser outlet was in fact providing sub-cooled liquid, thus allowing the pump to run as intended. Water-side flow rate to the evaporator was set to 17.5 $kg \cdot s^{-1}$ and 25°C water inlet temperature, while condenser water-side flow rate and inlet temperature varied as according to the set test matrix. As tests will show (in the test results section), the pump inlet must receive subcooled liquid, and this was not always provided by the condenser outlet, which sometimes came out as two phase. In order to account for this, a small 3 kW shell-and-tube heat exchanger was added to the outlet of the condenser, to act as a further sub-cooler, condensing the ammonia working fluid to a state where the pump could effectively pump it.

Figure 36: Shell-and-Tube Titanium Subcooler

This subcooler pictured in Figure 36 had chilled water provided to it by a stand-alone 15 kW chiller, sending 3-5°C water through it in order to cool the ammonia to a liquid level before entering the pump. Once water-side flow rates were fixed, a working fluid mass flow rate was also fixed, according to the test matrix. Once all conditions reached their steady states, each respective test was conducted, with differing values of working fluid and water flow rate, as well as inlet temperatures.

2.4 System Energy Balance

In order to accurately analyze system performance, energy balances for both PHE's were critical, as an imbalance in capacity between working fluid and water-side meant improper insulation, or an error in instrument measurement points. Water-side cooling and heating capacities were calculated based upon measured values of water mass flow rate, specific heat at appropriate temperature and atmospheric pressure, and temperature difference measured across each respective heat exchanger, as shown in equation (5)

$$\dot{Q}_{water} = \dot{m} * c_p * (T_{w,i} - T_{w,o}) \quad \textbf{(5)}$$

Working fluid side capacities were calculated using measured temperatures and pressures at the PHE inlet/outlet to calculate enthalpy values, which were then used in equation (6) for capacity calculations.

$$\dot{Q}_{Working\ Fluid} = \dot{m} * \Delta h_r \quad \textbf{(6)}$$

The working fluid side capacity calculations only held true when inlet and outlet state points were in the subcooled and superheated regions, as known temperatures and pressures could be used to calculate the corresponding enthalpy values. Once superheat was not available at higher working fluid mass flow rates, the water-side was solely relied upon for heat transfer coefficient (U value) calculations. Energy balance calculations for both PHE's were identical for both water and working fluid-side, where water side was relied upon in cases where superheating or subcooling regions were not present in the PHE's.

Energy balance was calculated as shown in equation (7).

$$\epsilon = \left(1 - \frac{\dot{Q}_{water}}{\dot{Q}_{ref}}\right) * 100\% \quad \textbf{(7)}$$

Energy balance figures and loss of superheating region with increased flow rates are presented in the Chapter 3: Test Results and Analysis section in further detail.

2.5 Uncertainty Analysis

Uncertainty analysis was conducted in order to determine the accuracy and error in measurements taken. Experimental uncertainty is composed of two components, systematic and random uncertainty. Systematic uncertainty is defined as reproducible innacuracies, which come from the measurement instrument. Systematic uncertainties are typically provided by the manufacturer for each given instrument, and are generally found in the form of a constant, or a percentage of the instrument reading. Instruments used with their corresponding systematic uncertainties are shown in Table 6.

Table 6: Instruments and Uncertainties

Measurement Instrument	**Unit**	**Instrument Uncertainty**
Pressure Transducer (Condenser)	kPa	0.862
Pressure Transducer (Evaporator)	kPa	4.3
Pressure Transducer Water (Cond/Evap)	kPa	0.862
Differential Pressure Water	kPa	0.17
Mass Flow Meter (Ammonia/Water)	-	0.1% of reading
RTD Condenser Working Fluid In/Out	°C	0.1
RTD Evaporator Working Fluid In/Out	°C	0.04
RTD Cond/Evap Water In/Out	°C	0.04

Random uncertainties encompass unknown and unpredictable changes in every data point recorded over the course of the testing period. Random uncertainty was calculated using standard deviation, which was then summed with the systematic uncertainty to obtain the total uncertainty for each sensor used.

Calculation of random and systematic uncertainties shown above was only applicable to directly recorded measurements. Other parameters which were calculated based

upon instrument measurements such as enthalpy and capacities used the Pythagorean summation in order to calculate uncertainty, shown in equation **(8)**.

$$\omega_h = \sqrt{\left(\frac{\partial h}{\partial P}\omega_P\right)^2 + \left(\frac{\partial h}{\partial T}\omega_T\right)^2} \quad \textbf{(8)}$$

In order to calculate the partial derivatives of enthalpies with respect to pressures and temperatures, a different method other than direct differentiation was taken, utilizing the difference between maximum and minimum pressures and temperatures. The corresponding max/min pressures and temperatures were defined by equations (9) and (10).

$$P_{max/min} = P_{measured} \pm \omega_P \quad \textbf{(9)}$$

$$T_{max/min} = T_{measured} \pm \omega_T \quad \textbf{(10)}$$

Similarly, enthalpies were calculated by equations (11) and (12).

$$\frac{\partial h}{\partial P} = \frac{h(P_{max}) - h(P_{max})}{P_{max} - P_{min}} \quad \textbf{(11)}$$

$$\frac{\partial h}{\partial T} = \frac{h(T_{max}) - h(T_{max})}{T_{max} - T_{min}} \quad \textbf{(12)}$$

Uncertainties for other variables were also calculated using a similar method. Measured variable values for one randomly selected condenser test are shown in Table 7, along with their corresponding calculated errors. Measured relative error values were shown to be kept below 1%, while calculated variables such as water-side capacity and LMTD were kept below 5%. The highest relative error came from the U-value calculation, which had a 6.3% relative error.

Table 7: Calculated Error Values

Variable	Unit	Measured Value	Total Error	Relative Error
Ammonia MFR	$g \cdot s^{-1}$	40.1	0.04	0.09%
Water MFR	$kg \cdot s^{-1}$	3.0	0.003	0.10%
$T_{w,in}$	°C	12.03	0.1	0.83%
$T_{w,out}$	°C	15.34	0.1	0.07%
$T_{ref,in}$	°C	15.45	0.04	0.26%
$T_{ref,out}$	°C	13.62	0.04	0.29%
$P_{ref,in}$	kPa	738.5	0.862	0.11%
$P_{ref,out}$	kPa	735.0	0.862	0.11%
$h_{ref,in}$	$kJ \cdot kg^{-1}$	1477.0	0.139	0.01%
$h_{ref,out}$	$kJ \cdot kg^{-1}$	263.7	0.188	0.07%
Q_{water}	kW	41.61	1.8	4.3%
LMTD	K	1.64	0.075	4.4%
$U\text{-Value}_{condenser}$	$W \cdot m^{-2} \cdot K^{-1}$	1291.8	81.3	6.3%

3. Test Results and Analysis

3.1 System Energy Balance

The energy balance concerning heat transfer between the water and working fluid-side plays an important part in system analysis. Therefore, energy balance was looked at for each test conducted on the condenser side, to ensure that working fluid and water-side match within 5% of each other. As working fluid mass flow rate was increased for various tests, the presence of superheat at the evaporator outlet vanished. Therefore, at higher working fluid MFR, energy balance was not applicable, as the evaporator outlet point was in two-phase, where enthalpy values and capacity could not be calculated. For these test cases, the water-side was relied upon to be an accurate measure of the system capacity.

In order to validate the accuracy of using only water-side capacity as a reference, ammonia MFR was gradually increased in small increments of 2 $g \cdot s^{-1}$ (with superheating present) until no more superheating existed. All tests conducted in region with superheating available showed energy balances of water-and working fluid-side that fell at or below 3%. Typical values for any given test are shown in Table 8.

Table 8: Energy Balances Water-Refrigerant (Condenser)

Test	Water-Side Capacity (kW)	Working Fluid-Side Capacity (kW)	Energy Balance (%)
1	37.5	38.1	1.60
2	39.4	40	1.52
3	42.4	42.7	0.71
4	44.1	45.1	2.27
5	37.1	37.9	2.16
6	43.5	43.7	0.46
7	36.7	37.5	2.18
8	43.1	43.7	1.39
9	36.7	37.4	1.91
10	42.3	42.8	1.18

All cases where superheating allowed for proper energy balance were averaged, which resulted in an average energy balance of 1.54% for all cases, well below the target 5% stated earlier. Due to the good energy balance, water-side capacity was shown to be accurate in regions where working fluid-side calculations were not applicable.

Energy balance for the evaporator side was also considered, to ensure proper calculations were being conducted and heat was being transferred as it should across the PHE's. Table 9 shows a similar chart of water-versus working fluid-side capacities for the evaporator, which show less than 5% deviation for multiple tests, ensuring that heat losses were not extreme for both PHE's.

Table 9: Energy Balance Water-Refrigerant (Evaporator)

Test	Water-Side Capacity (kW)	Refrigerant-Side Capacity (kW)	Energy Balance (%)
1	37.4	38.2	2.14
2	43.5	44.5	2.30
3	37.5	38.3	2.13
4	42.8	44.2	3.27

Figure 37 demonstrates that working fluid entering the condenser is in fact in the super-heated region for all MFR's, and is not entering as two-phase working fluid. Therefore, condenser working fluid-side capacity can be trusted, and as shown in section 2.4, both the working-fluid and water-side capacities matched within 5% for the condenser.

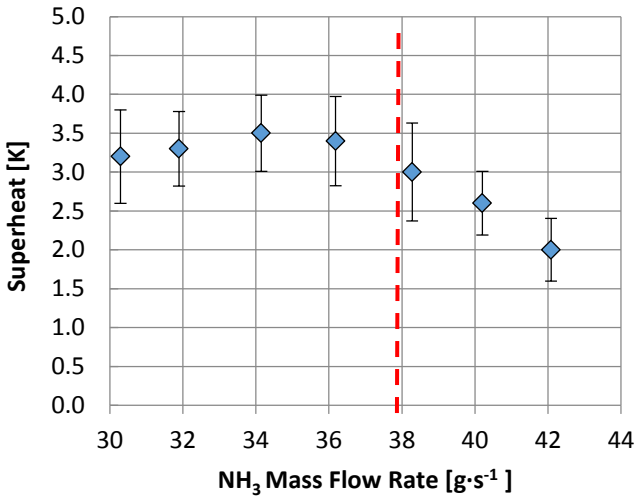

Figure 37: Superheat at Condenser Inlet

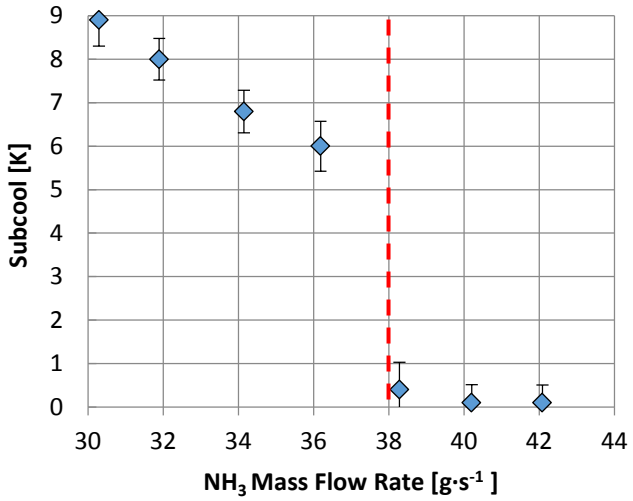

Figure 38: Subcooling at Condenser Outlet

However, this is not the case with the condenser outlet, shown in Figure 38, which displays high levels of subcooling at lower ammonia MFR, but rapidly diminishes as flow rate is increased. The transition period at which the sub-cooling ceases to exist is promptly after 36 $g \cdot s^{-1}$ of ammonia flow rate, and thus after this point only water side capacity was used for calculation of the heat transfer coefficient, as the quality exiting the condenser was unknown and could not be calculated. In order to address potential problems of not enough liquid feed to the pump, an additional chiller and subcooler of 3 kW was added to avoid this problem.

3.2 Overall Heat Transfer Coefficient of Condenser

The objective of the test was to understand how performance of the PHE was affected by varying working fluid mass flow rate, water-side flow rate, and water inlet temperature. Performance of the PHE was discussed in terms of the overall heat

transfer coefficient (U-value) and capacity, which was calculated using the following equations:

$$\dot{Q} = U * A * LMTD \quad \textbf{(13)}$$

Rearranging, the equation for overall HTC is:

$$U = \frac{\dot{Q}}{A * LMTD} \quad \textbf{(14)}$$

LMTD along with a known capacity and PHE heat transfer area was used to back-calculate the overall heat transfer coefficient value.

$$LMTD = \frac{\Delta T_1 - \Delta T_2}{ln\Delta T_1 - ln\Delta T_2} \quad \textbf{(15)}$$

Where:

$$\Delta T_1 = T_{ref,in} - T_{water,out} \quad \textbf{(16)}$$

$$\Delta T_2 = T_{ref,out} - T_{water,in} \quad \textbf{(17)}$$

In order to stay consistent for comparisons between heat transfer coefficient values, only the water-side capacity was used (not the working fluid-side) in the U-calculation. As explained earlier, this is due to the fact that at higher ammonia flow rates, superheat ceases to exist (evaporator side), and subcooling out of the condenser vanishes, which doesn't allow for proper calculation of refrigerant side capacity

without knowing the quality (there was no way to determine the ammonia quality in the two phase region).

Also shown earlier were the matching energy balances between working fluid and water-side (condenser) at lower flow rates below 5%, which validates that water-side calculation can be trusted for further HTC calculations.

Figure 39 and Figure 40 show the effect of increasing working fluid mass flow rate on U-value and capacity for the PHE condenser, while water MFR and water inlet temperature were kept constant.

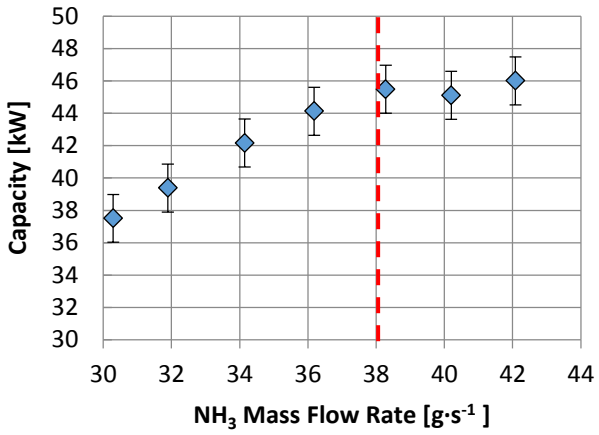

Figure 39: Condenser Capacity versus Ammonia Mass Flow Rate

The overall increase in ammonia MFR was from 30 $g \cdot s^{-1}$ up to 42 $g \cdot s^{-1}$ (a 40% increase), which saw the system capacity increase 8 kW from 38 kW to 46 kW. As expected, the two are directly correlated, as capacity increased with increasing ammonia flow rate. Capacity increase falls off around 38 $g \cdot s^{-1}$ working fluid flow rate, due to subcooling decreasing to values near zero (previously shown), indicating

the condenser outlet is in two-phase region, as shown in the area right of the dashed red line. Condenser capacity was expected to keep increasing once working fluid was in two-phase region, however due to increasing of water inlet temperature due to chiller limitations as shown by Figure 42, LMTD was not as high as expected. This lowered LMTD from the expected value contributes to a stabilizing of condenser capacity, which should instead see an increase in capacity while in two-phase region. U-value was left mostly unchanged and constant as all values in two-phase region (all values remain within the error range) as ammonia MFR was increased, which can only be attributed to an increase in the LMTD as shown in Figure 41. Capacity increases as expected when LMTD was increased, and follows the same trend of falling off once condenser subcooling is non-existant, and the condenser outlet is in two-phase area.

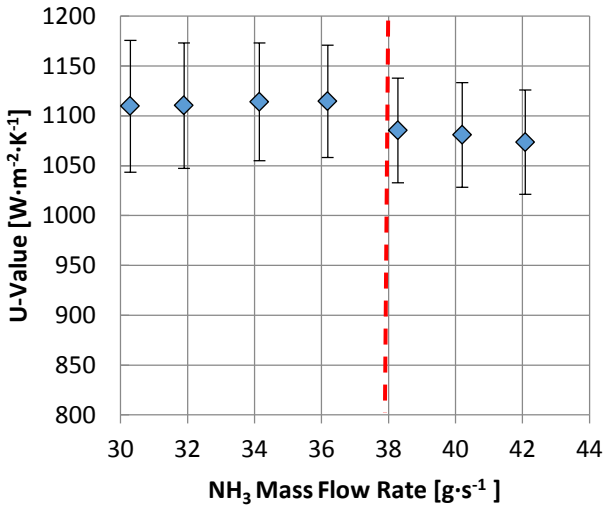

Figure 40: Overall Heat Transfer Coefficient versus Ammonia Mass Flow Rate

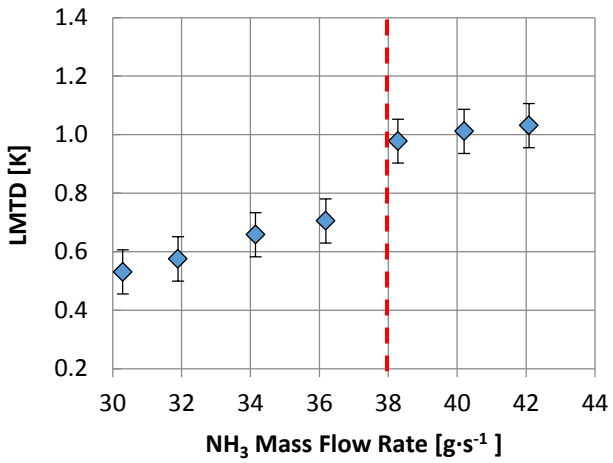

Figure 41: LMTD versus Ammonia Mass Flow Rate

Figure 41 displays the change in LMTD as working fluid flow rate was increased. As MFR NH_3 was increased, LMTD gradually began to increase, but as shown by Figure 42 condenser water inlet temperature was not held at the ideal inlet of 8.0°C as capacity was increased, due to limitations on the outdoor chiller side. Due to the increase in condenser water-side inlet temperature, LMTD was slightly affected, thus not producing a completely linear increase as was the trend with capacity. As previously explained, once NH_3 MFR reaches approximately 38 $g \cdot s^{-1}$ and subcooling of condenser is no longer available (two-phase region), LMTD stops increasing as quickly as it should (due to increase in water inlet temperature) and thus capacity follows the same trend, of becoming nearly constant in the two-phase region. Expected LMTD should be higher than shown in Figure 41, but due to the increase in water inlet temperature pictured in Figure 42 (compared to ideal constant value of

8°C), LMTD values shown are lower than they should be, leading to a falling-off of capacity when it should keep increasing in the two-phase region.

Figure 43 displays the ΔT1 and ΔT2 used in the calculation for the LMTD. As shown in Figure 41, LMTD shows a large increase at higher flow rates, due to the decrease of ΔT1 and the increasing ΔT2. The LMTD variation is due to the mixed effect of the respective inlet-outlet temperature differences, where the decrease from ΔT1 and increase in ΔT2 happen at different rates, leading to the non-linear trend displayed by Figure 41 for LMTD. The different rates of temperature difference increase was due to a non-ideal increase in water inlet temperature, as depicted in Figure 42.

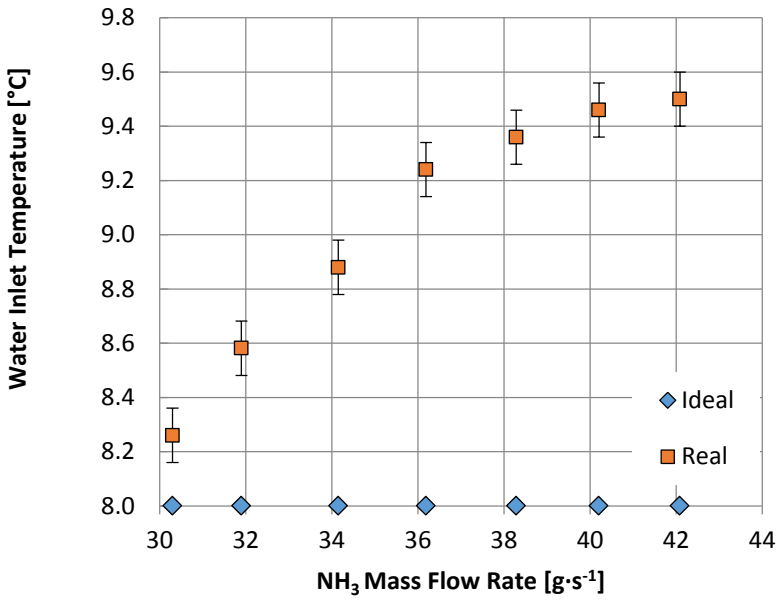

Figure 42: Condenser Water Inlet Temperature

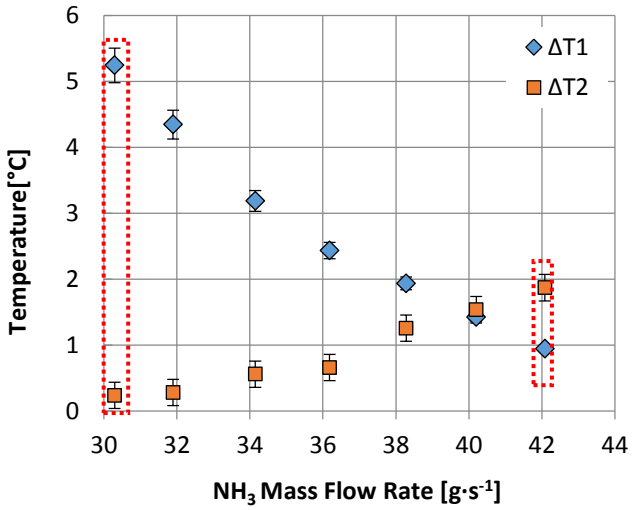

Figure 43: ΔT1 and ΔT2 for LMTD as NH_3 MFR was Varied

Figure 44 and Figure 45 display and confirm the trend previously shown in Figure 43, where working fluid and water operated in counter-flow. As ammonia MFR is increased from 30 $g \cdot s^{-1}$ to 42 $g \cdot s^{-1}$, ΔT1 (NH_3 inlet to water outlet) shows a constant decrease in temperature difference. Shown is the ammonia inlet temperature as it changed from left to right (30 $g \cdot s^{-1}$ on the left, 42 $g \cdot s^{-1}$ on the right), and similarly the water outlet temperature as it varied at the two extreme MFR's. In contrast, ΔT2 (H_2O inlet to NH_3 outlet) of Figure 45 shows that as NH_3 MFR is increased, this value starts small and increases, displaying the trend of increasing LMTD as ammonia MFR is increased.

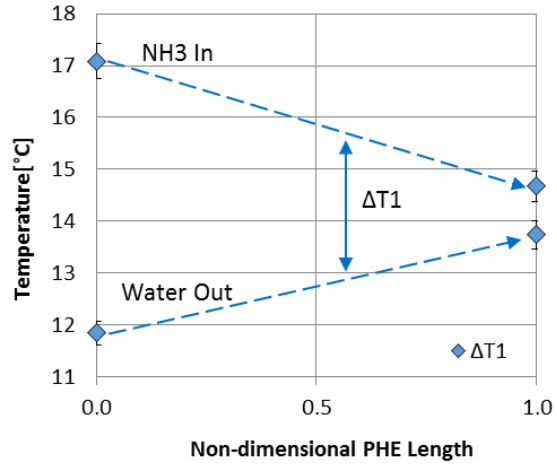

Figure 44: ΔT1 Across PHE as NH_3 at 30 g·s^{-1} and 42 g·s^{-1}

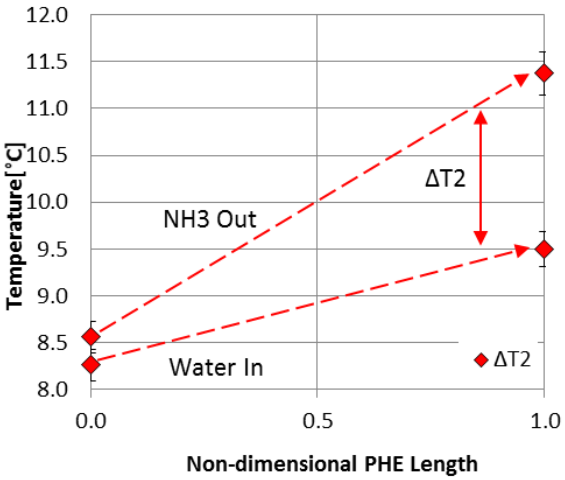

Figure 45: ΔT2 Across PHE as NH_3 at 30 g·s^{-1} and 42 g·s^{-1}

Figure 46 shows the temperature varied as ammonia MFR was increased from 30 g·s^{-1} to 42 g·s^{-1}. All four streams are shown, including ammonia inlet and outlet streams as well as water inlet and outlet. The water inlet temperature (red diamonds) as previously shown was not kept constant at 8.0°C, and thus increased to 9.5°C with increasing ammonia MFR. This had a significant impact on water and ammonia outlet temperatures, which were both increased with increasing ammonia MFR. Control over decreasing ammonia inlet temperature was due to extraneous parameters, and was not affected by the increase in water inlet temperature.

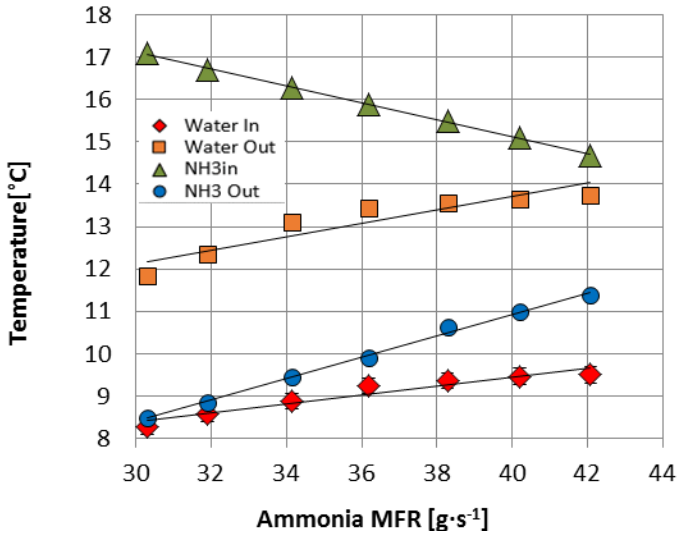

Figure 46: NH_3 and H_2O inlet/outlet streams at 30 g·s^{-1} and 42 g·s^{-1}

Figure 47 displays a comprehensive figure with the effects of increasing ammonia MFR and increasing water inlet temperature on ΔT1 and ΔT2. Variables kept constant were the water MFR and water inlet temperature (as controlled by the chiller). Plotted in the red line is the difference between ΔT1 and ΔT2 through the PHE at 30 g·s^{-1} NH_3 MFR, where ΔT1 is shown on the right and ΔT2 on the left, as the PHE operates in counter-flow. The red cycle depicts ΔT1 as it starts large and becomes small as confirmed by Figure 44 and Figure 45 on the respective left-side of the graph (the left side represents ΔT1 and ΔT1 at 30 g·s^{-1} NH_3 MFR). Shown in blue is the cycle as ammonia MFR was increased to 42 g·s^{-1}. In contrast to ΔT patterns exhibited at 30 g·s^{-1} NH_3 MFR (red line), the blue line demonstrates that ΔT1 becomes small when compared to ΔT1 of 30 g·s^{-1} NH_3 MFR, and ΔT2 becomes larger when compared to the smaller NH_3 MFR. The decrease in ΔT1 and increase in ΔT2 at 42 g·s^{-1} NH_3 MFR is confirmed by Figure 44 and Figure 45.

Figure 47 clearly depicts the difference in impact that ammonia MFR and increasing water inlet temperature (due to non-perfect chiller control) had on ΔT's through the PHE, which will consequently impact overall LMTD.

In conclusion, Figure 47 effectively depicts the rate at which ΔT1 decreases with increasing NH_3 MFR, and how ΔT1 is then adversely affected by the increasing water inlet temperature.

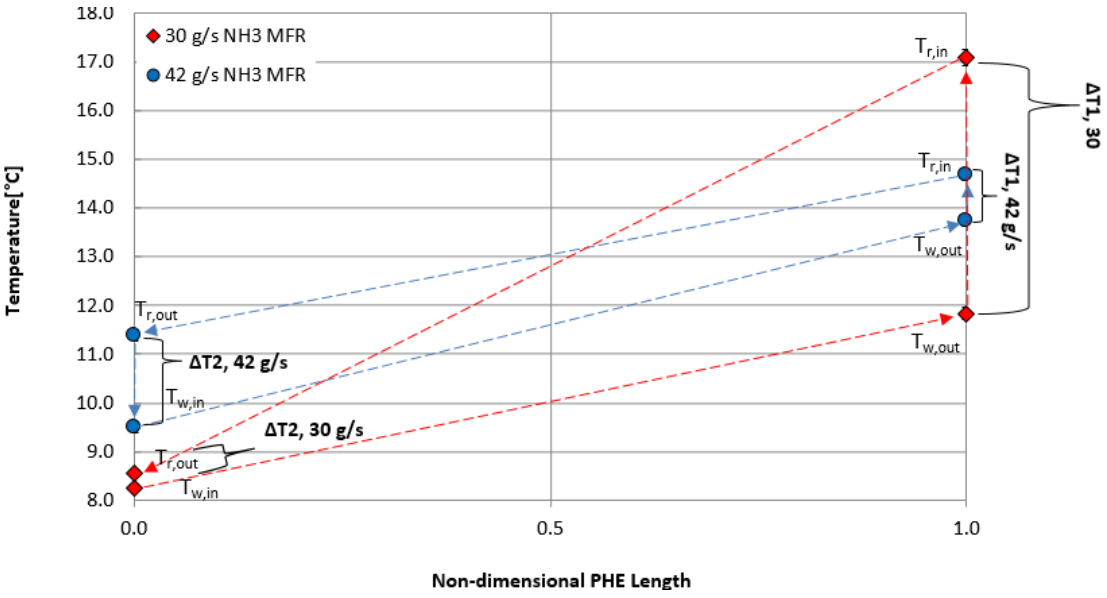

Figure 47: ΔT1 and ΔT2 Across PHE at 30 g·s^{-1} and 42 g·s^{-1}

Capacity and U-values were most heavily influenced by water-side flow rate, as shown in Figure 48 and Figure 49, where water inlet temperature and ammonia MFR were kept constant (ammonia was kept constant at three different MFR's). Water flow rate to the condenser was varied from 2.0 kg·s^{-1} up to 3.0 kg·s^{-1}, while average water inlet temperature was approximately held to 9°C.

When water flow rate was increased, capacity saw a linear increase for tests conducted at both 35 g·s^{-1} and 40 g·s^{-1} of NH_3 MFR. The only exception was at lower

flow rates, namely 30 $g \cdot s^{-1}$, where condenser capacity remained unchanged. This is due to MFR of the working fluid being very low, and not having a sizeable impact on capacity at such low flow rates.

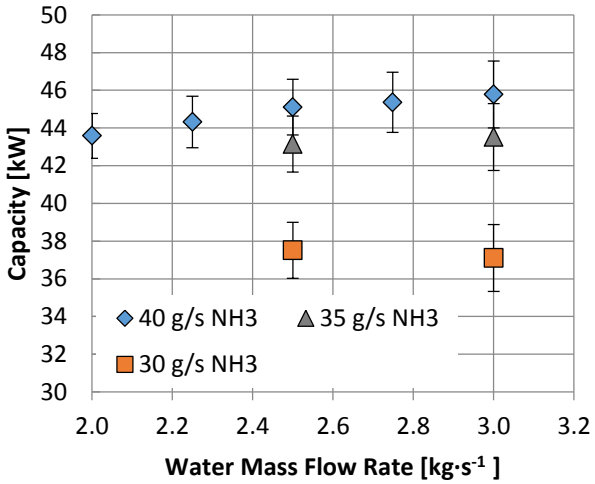

Figure 48: Capacity versus Water Mass Flow Rate

Overall HTC shown in Figure 49 was affected drastically by increasing water-side flow rate, with a linear increase for all three test cases, namely 30, 35, and 40 $g \cdot s^{-1}$ of NH_3 MFR. U-Value was shown to be in a similar value range at 3.0 $kg \cdot s^{-1}$ water flow rate, independent of working fluid-side MFR. Water inlet temperature was held constant for all tests completed (with the exception of 8°C water inlet, which was due to chiller limitations), in order to accurately monitor performance of one variable at a time.

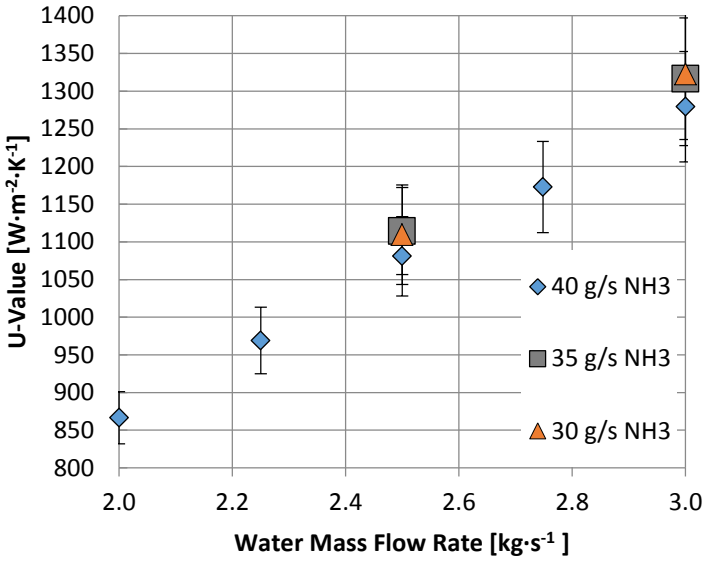

Figure 49: Heat Transfer Coefficient versus Water Mass Flow Rate

Figure 50 displays the effect water mass flow rate coupled with three different working fluid flow rates had on condenser LMTD. As water flow rate was increased, LMTD saw little to no change for 30 $g \cdot s^{-1}$ and 35 $g \cdot s^{-1}$ NH_3 flow rate, respectively, while 40 $g \cdot s^{-1}$ displayed a minor decrease of approximately 0.1°C. Increasing water-side flow rate had an overall neutral effect on LMTD, showing little or no change. However, increasing or decreasing the NH_3 MFR had a slight impact at higher flow rates, while remaining unchanged at lower NH_3 MFR's.

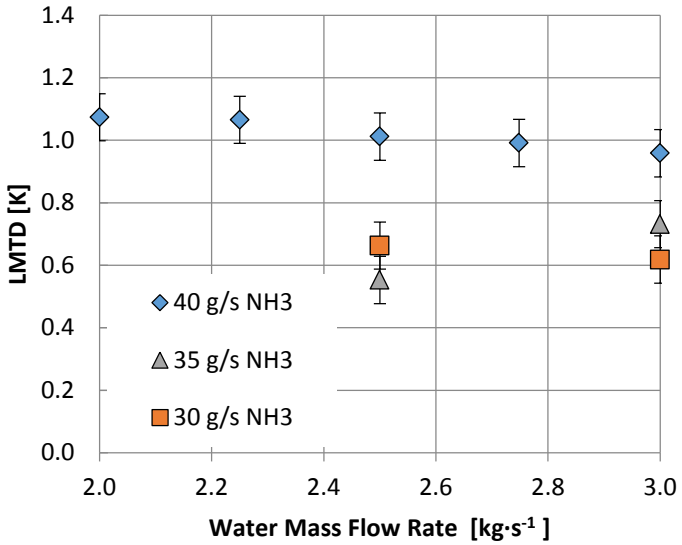

Figure 50: LMTD versus Water Mass Flow Rate

The final set of tests involved varying the water inlet temperature from 8°C to 12° in increments of two degrees, in order to assess the effect of increasing water temperature across the PHE condenser. The fixed variables in these cases were the water MFR and ammonia MFR's. The general trend across all working fluid flow rates in Figure 51 shows a decrease in capacity as water inlet temperature is increased, as expected. This will decrease LMTD values, and as such capacity will also decrease, regardless of working fluid flow rates.

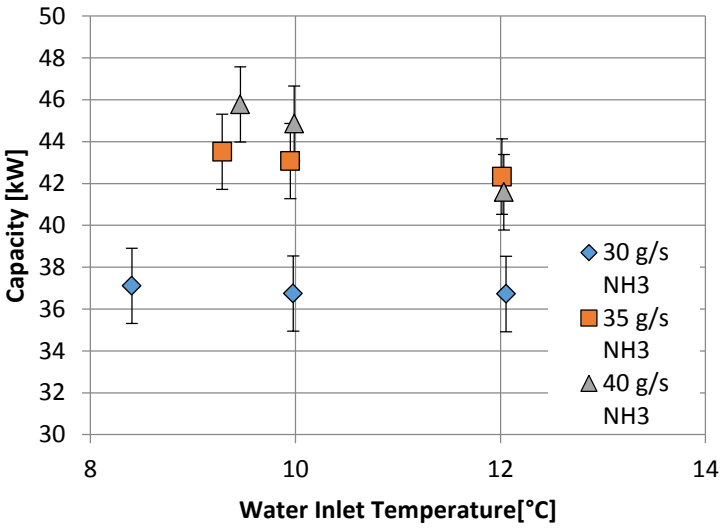

Figure 51: Capacity versus Water Temperature

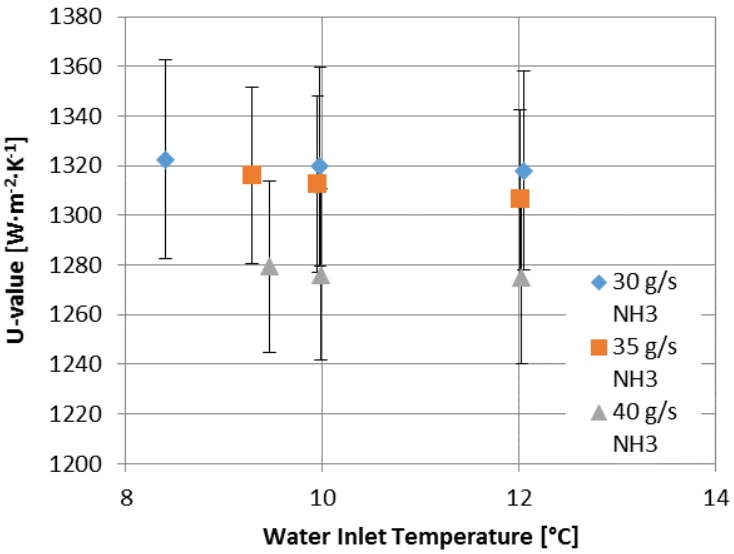

Figure 52: Overall Heat Transfer Coefficient versus Inlet Water Temperature

Results shown in Figure 52 and Figure 53 display that increasing water inlet temperature has a marginal effect on capacity and heat transfer coefficient. As

expected, increasing water temperature decreases system performance (capacity drops slightly). This effect is shown to be more drastic at larger flow rates (35 $g \cdot s^{-1}$ and 40 $g \cdot s^{-1}$), while the tests at 30 $g \cdot s^{-1}$ showed little to no decreases in system capacity.

Figure 53 shows that at all NH_3 MFR's, LMTD was heavily affected by increasing the condenser water inlet temperature. LMTD dropped almost linearly across all flow rates, indicating that the slight increase in water inlet temperature has a large effect on performance, as LMTD decreased by approximately 15% in all cases for a 3°C increase in water temperature.

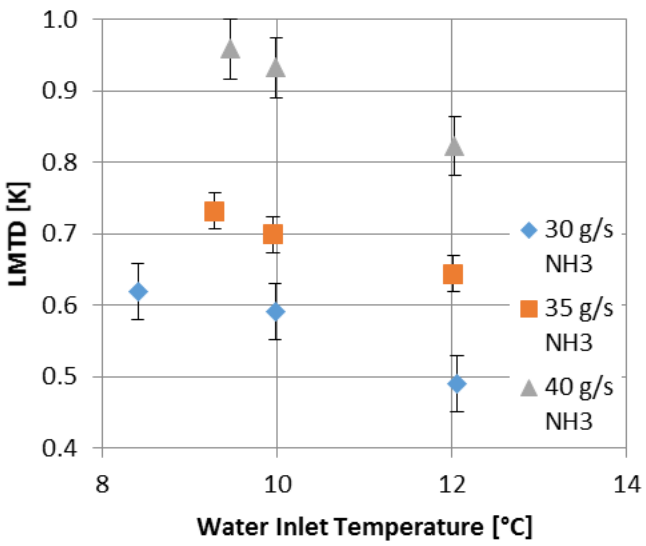

Figure 53: LMTD versus Water Inlet Temperature

3.3 PHE Pressure Drop

While analysis of heat transfer coefficient and capacity display the performance values in terms of heat transfer of the PHE, pressure drop plays a significant portion of cycle performance, as its influence affects pumping power required, which can increase or decrease cycle efficiency. Both water and working fluid-side pressure drops were recorded, using the difference between two absolute pressure transducers placed at respective condenser inlets and outlets for the most accurate readings.

Shown in Figure 54, the working fluid-side pressure drop was measured and plotted as ammonia flow rate was gradually increased, in small steps of 2.0 $g \cdot s^{-1}$ per trial. The graph shows that the pressure drop increase was non-linear, but kept below 4.5 kPa at the highest ammonia MFR tested. The pressure drop through the PHE is linear when working fluid exits as subcooled liquid, but pressure drop increases exponentially once subcooling ceases to exist, and working fluid is in the two-phase region, as demonstrated by flow rates larger than 36 $g \cdot s^{-1}$.

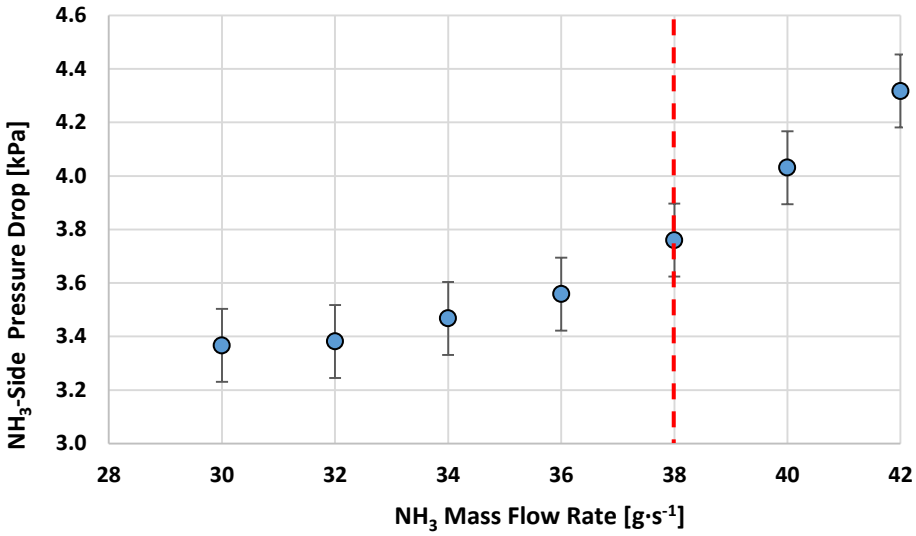

Figure 54: Working Fluid-Side Pressure Drop across Condenser versus Ammonia Mass Flow Rate

The final Figure 55 demonstrates the behavior of water side pressure drop as the water-side flow rate was increased. In contrast to the ammonia MFR, water side-pressure drop increased linearly when water flow rate was linearly increased, albeit at a slightly higher pressure drop than the working fluid-side, in the range of 6 to 8 kPa. Knowledge of both working fluid-side and water-side pressure drops is critical when applying this to OTEC PHE plate design, as capacity versus pressure drop must be accounted for.

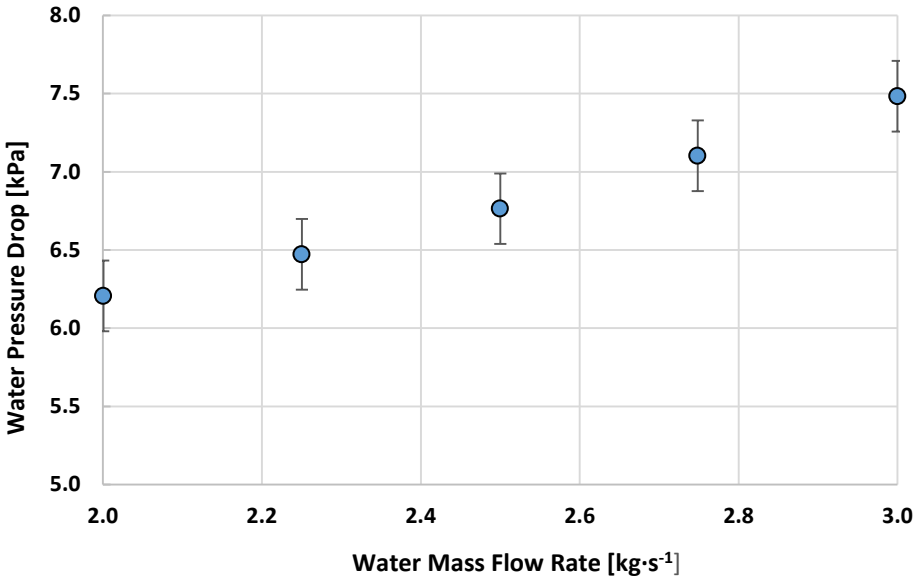

Figure 55: Water-Side Pressure Drop versus Water MFR

4. Conclusions

4.1 Summary of Accomplishments

The PHE experimental performance analysis when used as an ammonia condenser in a power generation cycle showed how performance was affected by varying three variables, namely ammonia flow rate, water flow rate, and condenser water inlet temperature. This experimental analysis was limited to testing of the semi-welded PHE with ammonia as the working fluid. While other researchers are developing new types of heat exchangers applicable to the OTEC cycle, the PHE instrumented and tested was a commercially available off-the-shelf heat exchanger.

Test findings showed that the least influential parameter was the water inlet temperature, which had a small effect on both capacity and heat transfer coefficient when varied from 8°C to 12°C, a four degree increase. Capacity performance was decreased for all working fluid flow rates tested when water inlet temperature was

increased. This had a neutral effect on overall HTC, as it neither increased nor decreased it, but showed it decreased the LMTD as the temperature rose.

The second most influential parameter was ammonia flow rate, which when increased from 30 $g \cdot s^{-1}$ to 42 $g \cdot s^{-1}$ showed a substantial increase in both heat exchanger capacity and LMTD, however overall HTC wasn't substantially increased. Results showed a linear increase in condenser capacity when ammonia MFR was increased, however at higher flow rates when subcooling was not available and condenser outlet was in the two-phase region, increasing NH_3 flow rate showed to have little to no impact on capacity. A similar trend was shown for LMTD, which dropped off and stopped increasing after condenser outlet reached the two-phase region instead of exiting as subcooled liquid.

The most influential variable was shown to be water flow rate. PHE capacity was held nearly constant and wasn't vastly affected. When increasing water flow rate however, LMTD saw a linear decrease only for the highest NH_3 MFR of 40 $g \cdot s^{-1}$, while secondary flow rates of 35 $g \cdot s^{-1}$ and 30 $g \cdot s^{-1}$, respectively were not affected. When water flow rate was increased by 50%, from 2.0 $kg \cdot s^{-1}$ up to 3.0 $kg \cdot s^{-1}$, overall HTC was increased almost linearly by approximately 45%, showing it to have the largest increased and impact on overall HTC of the tested PHE when compared to variation of ammonia MFR and water inlet temperature.

Testing of the semi-welded PHE as an ammonia condenser showed it exhibits low pressure drop for both working fluid-side and water-side, as well as having good heat transfer capabilities in terms of capacity and overall heat transfer coefficient. When compared to the brazed PHE tested by Leighton et al, pressure drop at similar

working fluid MFR's showed the brazed PHE to have approximately 50% higher pressure drop. The combination of excellent heat transfer, and compact size make the semi-welded PHE a viable choice for an ammonia condenser, which could also be used in an OTEC ammonia cycle, as shown by testing at similar water temperature and working fluid pressure conditions.

Possible contributions to OTEC engineering planning and design include correct sizing of plates (number of plates required) for the heat exchanger based upon capacity tests. Testing of working fluid and water-side pressure drops also gives insight into OTEC pump sizing, for both the ammonia and water-side loops, which must account for the pressure drop seen across the PHE. Finally, the combination of system cost by correct sizing of the PHE plates and operational cost by loss in pressure drop across the PHE can be optimized in order to offer the best performance between plate heat transfer and pressure drop to yield highest cycle efficiency.

4.2 Future Work

Further future work could include regulation of inlet quality into the condenser with the use of a pre-condenser heat exchanger. This could serve many purposes, which includes detailed analysis of heat transfer at different inlet qualities, and a more comprehensive analysis of heat transfer performance of the PHE condenser when working fluid enters as two-phase as opposed to vapor.

An increase in both PHE capacities by upgrading the limited chiller and pool heater loops could also test the limits of the PHE condenser, which was currently not available due to the limitations of both cold and warm water loops. This would aid in

discovering the maximum performance limits of the PHE, which were not investigated thoroughly in the tests conducted.

Finally, with unlimited time and resources, the performance of the PHE could be investigated based upon variation of plate parameters, such as number of plates, plate thickness, and variables such as chevron angle, width, and depth. This study would further extend the knowledge of how this PHE performance under various operating conditions and plate geometries.

5. References

[1] J.I. Yoon, C.H. Son, S.M. Baek, H.J. Kim, H.S. Lee, Performance characteristics of the R744 OTEC power cycle with its operation parameters, J. Korean Soc. Mar. Eng. 36 (2010) 13-20.

[2] J.I. Yoon, C.H. Son, S.M. Baek, H.J. Kim, H.S. Lee, Efficiency comparison of subcritical OTEC power cycle using various working fluids, Heat Mass Transfer 50 (2014) 985-996.

[3] H.S. Lee, H.J. Kim, D.H. Jung, D.S. Moon, A study on the improvement of the cycle efficiency of the closed-type OTEC, J. Korean Soc. Mar. Eng. 35 (2011) 46e52.

[4] J.I. Yoon, C.H. Son, S.M. Baek, H.J. Kim, H.S. Lee, Exergy analysis of the R744 OTEC power cycle with its operation parameters, J. Korean Soc. Mar. Eng. 36 (2012) 1036-1043.

[5] Z. Shengjun, W. Huaixin, G. Tao, Performance comparison and parametric optimization of the subcritical organic rankine cycle (ORC) and the transcritical power cycle system for low-temperature geothermal power generation, Appl. Energy 88 (2011) 2740-2754.

[6] A. Etemadi, A. Emdadi, O. AsefAfshar, Y. Emami, Electricity generation with ocean thermal energy, Energy Procedia 12 (2011) 936-943.

[7] N.J. Kim, C.N. Kim, W. Chun, Using the condenser effluent from a nuclear power plant for ocean thermal energy conversion (OTEC), Int. Commun. Heat Mass Transfer 36 (2009) 1008-1013.

[8] A.I. Kalina, Combined-cycle system with a novel bottoming cycle, J. Eng. Gas Turbines Power 106 (1984) 737-742.

[9] J. Bao, L. Zhao, Exergy analysis and parameter study on a novel auto-cascade rankine cycle, Energy 48 (2012) 539-547.

[10] X. Li, C. Zhao, X. Hu, Thermodynamic analysis of the organic rankine cycle with an ejector, Energy 42 (2012) 342-349.

[11] H. Uehara, Y. Ikegami, T. Nishida, Performance analysis of OTEC system using a cycle with absorption and extraction processes, Trans. Jpn. Soc. Mech. Eng. (Part B) 64 (1998) 384-389.

[12] Aspen HYSYS, Version 8.0, Aspen Technsology Inc., 2013.

[13] Ayub, Z. H. Plate heat exchanger literature survey and new heat transfer and pressure drop correlation for refrigerant evaporators. Heat Transfer Engineering, 24 (2003), 3-16.

[14] Energy Information Administration, U.S Department of Energy, 2014. Annual Energy Review 2014, Primary Energy Overview, Selected Years, 1980-2012.

[15] Energy Information Administration, U.S. Department of Energy, 2011. Annual Energy Review 2011, Primary Energy Production by Source, Selected Years, 1980-2012.

[15] Faizal, M., Ahmed, M. R. Experimental studies on a corrugated plate heat exchanger for small temperature difference applications. Experimental Thermal and Fluid Science, 36 (2012), 242-248.

[16] Fernandes, C, S., Dias, R, P., Nobrega, J, M., Maia, J, M. Laminar flow in chevron-type plate heat exchangers: CFD analysis of tortuosity, shape factor and friction factor. Chemical Engineering and Processing, 46 (2007), 825-833.

[17] Fernandez-Seara, J., Uhia, F, J., Sieres, J., Campo, A. A general review of the Wilson plot method and its modifications to determine convection coefficients in heat exchange devices. Applied Thermal Engineering, 27 (2007), 2745-2757.

[18] Han, D. H., Lee, K. J., Kim, Y. H. Experiments on the characteristics of evaporation of R410A in brazed plate heat exchangers with different geometric configurations. Applied Thermal Engineering, 23 (2003), 1209-1225.

[19] Han, X. H., Cui, L. Q., Chen, S. J., Chen, G. M., Wang, Q. A numerical and experimental study of chevron, corrugated plate heat exchangers. International Communications in Heat and Mass Transfer, 37 (2010), 1008-1014.

[20] Hsieh, Y.Y., Lin, T. F. Evaporation heat transfer and pressure drop of refrigerant R-410A flow in a vertical plate heat exchanger. Journal of Heat Transfer, 125 (2003), 852-857.

[21] Huang, J., Sheer, T, J., Bailey-McEwan, M. Heat transfer and pressure drop in plate heat exchanger refrigerant evaporators. International Journal of Refrigeration, 35 (2012), 325-335.

[22] Khan, T. S., Khan, M. S., Chyu, M. C., Ayub, Z. H. Experimental investigation of evaporation heat transfer ad pressure drop of ammonia in a 60o chevron plate heat exchanger. International Journal of Refrigeration, 35 (2012), 336-348.

[23] Khan, T. S., Khan, M. S., Chyu, M. C., Ayub, Z. H. Experimental investigation of single phase convective heat transfer coefficient in a corrugated plate heat exchanger for multiple plate configurations. Applied Thermal Engineering, 30 (2010), 1058-1065.

[24] Longo, G, A. Heat transfer and pressure drop during HFC refrigerant saturated vapor condensation inside a brazed plate heat exchanger. International Journal of Heat and Mass Transfer, 53 (2010), 1079-1087.

[25] Ma, H., Oxley, L., Gibson, J., China's energy situation in the new millennium. Renewable and Sustainable Energy Reviews, 13 (2009), 1781-1799.

[26] Martin, H. A theoretical approach to predict the performance of chevron-type plate heat exchanger. Chemical Engineering and Processing, 35 (1996), 301-310.

[27] Taboas, F., Valles, M., Bourouis, M., Coronas, A. Flow boiling heat transfer of ammonia/water mixture in a plate heat exchanger. International Journal of Refrigeration, 33 (2010), 695-705.

[28] Wellsandt, S., Vamling, L. Heat transfer and pressure drop in a plate-type evaporator. International Journal of Refrigeration, 26 (2003), 180-188.

[29] Yan, Y. Y., Lin, T. F. Evaporation heat transfer and pressure drop of refrigerant R-134a in a plate heat exchanger. Journal of Heat Transfer, 121 (1999), 118-127.

[30] Muthuraman Subbiah.The Characteristics of Brazed Plate Heat Exchangers with Different Chevron Angles. Higher College of Technology, 2004.